CHEMISTRY OF MATERIALS

pubs.acs.org/cm Article

Exploring Ca−Ce−M−O (M = 3d Transition Metal) Oxide Perovskites for Solar Thermochemical Applications

Gopalakrishnan Sai Gautam, Ellen B. Stechel, and Emily A. Carter*

Cite This: Chem. Mater. 2020, 32, 9964−9982 Read Online

ACCESS | Metrics & More | Article Recommendations | SI Supporting Information

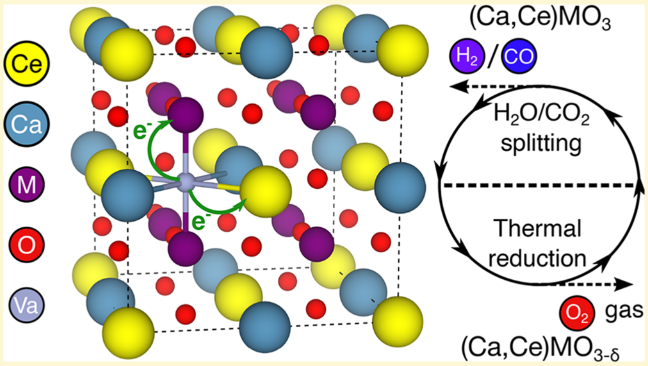

ABSTRACT: Solar thermochemical (STC) processes hold promise as efficient ways to generate renewable fuels, fuel precursors, or chemical feedstocks using concentrated sunlight. Specifically, one actively researched approach is the two-step STC cycle, which uses a redox-active, off-stoichiometric, transition-metal oxide material to split water and/or CO_2, generating H_2 and/or CO, respectively, or syngas (a combination of H_2 and CO). Identifying novel metal oxides that yield larger reduction extents (practically achievable off-stoichiometries) than the state-of-the-art CeO_2 is critical. Here, we explore the chemical space of Ca−Ce−M−O (M = 3d transition metal, except Cu and Zn) metal oxide perovskites, with Ca and/or Ce occupying the A site and M occupying the B site within an ABO_3 framework, as potential STC candidates. We use density functional theory (DFT)-based calculations and systematically evaluate the oxygen vacancy (Va_O) formation energy (≈ enthalpy of reduction in an STC cycle), electronic properties, thermodynamic stability of $CaMO_3$, $CeMO_3$, and $Ca_{0.5}Ce_{0.5}MO_3$ perovskites, and the Va_O formation energy within $Ca_{0.5}Ce_{0.5}Ti_{0.5}Mg_{0.5}O_3$ perovskite. We consider only Ca and/or Ce on the A site because of their similar size and the potential redox activity of Ce^{4+}. If both Ce and M exhibit simultaneous reduction with Va_O formation, the resulting perovskite could exhibit a larger entropy of reduction than a single cation reduction. The increased entropy produces increased reduction for fixed temperature, partial pressure of oxygen, and reduction enthalpy, and therefore increased STC efficiency. Importantly, we identify $Ca_{0.5}Ce_{0.5}MnO_3$, $Ca_{0.5}Ce_{0.5}FeO_3$, and $Ca_{0.5}Ce_{0.5}VO_3$ to be promising candidates based on their Va_O formation energy and thermodynamic (meta)stability. Moreover, based on our calculated on-site magnetic moments, electron density of states, and electron density differences between pristine and defective structures, we find $Ca_{0.5}Ce_{0.5}MnO_3$ to exhibit simultaneous reduction of both Ce^{4+} (A-site) and Mn^{3+} (B-site), highlighting a particularly promising candidate for STC applications with a predicted higher entropy of reduction than CeO_2. Finally, we extract metrics that govern the trends in Va_O formation energies, such as standard reduction potentials, and provide pointers for further experimental and theoretical studies, which will enable the design of improved materials for the STC cycle.

1. INTRODUCTION

Generating H_2 and/or CO using off-stoichiometric oxides via a two-step solar thermochemical (STC) process that splits water (STCH) and/or CO_2 (STCC) is a promising technological pathway to generate sustainable fuel and/or fuel (or chemical) precursors.[1,2,11,3−10] Sustainable fuel alternatives are particularly important for heavy-duty transportation or aviation, which are difficult to electrify, and for other applications aimed at achieving a net carbon-neutral economy. Briefly, typical STC cycles consist of two distinct steps,[5,9,12,13] namely, a thermal reduction (TR) step where an oxidized metal oxide is heated to high temperatures (>1673 K) and low oxygen partial pressures (p_{O_2} < 100 Pa) to induce oxygen deficiency/off-stoichiometry. Subsequently, the off-stoichiometric oxide cools to a lower temperature (873−1473 K; in the absence of a source of oxygen), where it spontaneously splits steam in the water-splitting (WS) reoxidation step. CO_2 splitting can replace the WS step to produce CO, or a combination of the two can generate a mixture of H_2 and CO.

However, new materials are required to increase the extent of reduction at similar or lower temperatures and thereby improve the efficiency of the STCH cycle, beyond the state-of-the-art pure CeO_2,[5,14−18] if STCH is to contribute meaningfully to future renewable fuels portfolios. Recently, oxide perovskites, which also appear in non-STC, energy-conversion devices,[19−25] have gained traction as potential candidates.[26,27,36−38,28−35] Several studies have reported improved

Received: July 13, 2020
Revised: November 1, 2020
Published: November 17, 2020

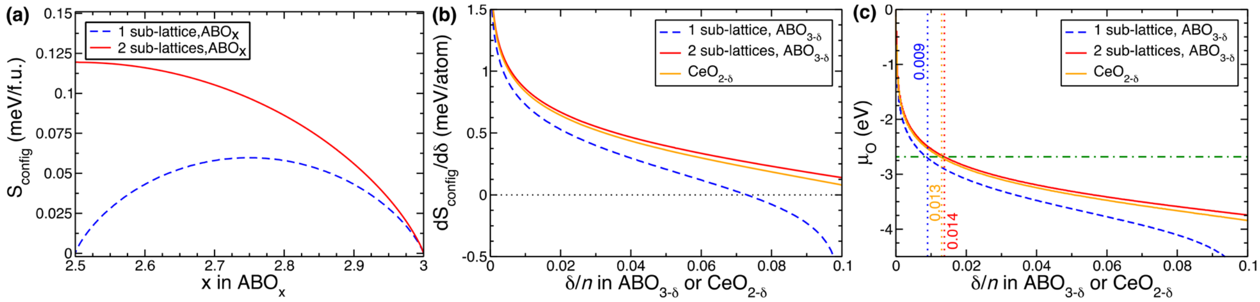

Figure 1. (a) Configurational entropy of reduction, including only the cation sublattice(s), plotted as a function of oxygen concentration (x in ABO_x) for scenarios involving single (dashed blue curve) and simultaneous (solid red curve) cation reduction. (b) Derivative of the configurational entropy with respect to oxygen off-stoichiometry (δ), plotted against δ normalized per number of atoms in stoichiometric ABO_3 or CeO_2 (n). The derivatives include both anion and cation sublattices. (c) Evolution of the oxygen chemical potential as a function of δ/n in $ABO_{3-\delta}$ and $CeO_{2-\delta}$, at a reduction enthalpy of 3.98 eV/Va_O. Dash-dotted green line represents chemical potential of oxygen gas at 1673 K and a p_{O_2} of 10^{-4} atm. Dotted red and blue lines signify equilibrium δ/n (or δ_{eq}/n) under the aforementioned conditions for an ABO_3 perovskite with and without simultaneous redox activity, respectively. Dotted orange line indicates δ_{eq}/n in $CeO_{2-\delta}$.

productivity metrics for water/CO_2 splitting.[27,28,39] Oxide perovskites are attractive candidates particularly because of the diversity of metal cations that can occupy the A and B sites within an ABO_3 framework, which provides a flexible handle to tune the enthalpy of reduction (ΔH_{red}, closely related to the oxygen vacancy formation energy, $E_f\,[Va_O]$[31]) to suit STCH/STCC processes.

A notable drawback of moving to a perovskite framework is the loss in entropy of reduction (ΔS_{red}) per oxygen or per atom compared to CeO_2.[17,40,41] Reduced CeO_2 exhibits configurational entropy within its two sublattices, the oxygen anion (O + Va_O, where Va_O = oxygen vacancy) and the Ce cation (Ce^{3+} + Ce^{4+}) sublattices.[42−44] Ce also can exhibit an on-site electronic entropy, due to the multitude of low-energy configurations available for electrons occupying the seven 4f orbitals,[17] which was used recently in a search of Ce-based materials for STCH and the subsequent proposal of $CeTi_2O_6$ as a candidate by Naghavi et al.[45] By contrast, an ABO_3 perovskite often has only one redox active cation, the B (typically, 3d transition metal) cation, thereby exhibiting configurational entropy only within one of two cation sublattices and the oxygen anion sublattice. Thus, the primary cause of the decrease in ΔS_{red} is the lack of redox-activity of the A cation. Additionally, the nonredox activity of A in ABO_3 reduces the oxygen evolution capacity, normalized per mol-atom of the oxide, since A only ensures the structural integrity of the perovskite framework without contributing to the redox process in an STC cycle. A higher ΔS_{red} results in a higher production of H_2 (CO) in water (CO_2) splitting per unit oxide (see Section 2) for the same enthalpy of reduction and would provide additional flexibility in the temperatures and/or partial pressures used for the TR and WS steps.[4,5,40,46] A potential way of increasing ΔS_{red} in oxide perovskites is to identify compositions where both A and B cations are simultaneously redox-active, as the reduction of both A and B furnishes additional configurational degrees of freedom to increase ΔS_{red}. Hence, if there are perovskite compositions that can exhibit simultaneous redox activity, that would introduce a new strategy for identifying a material class which could exceed the performance of ceria. Discovering such a material class is the focus of this work.

We explore herein the chemical space of Ca−Ce−M−O perovskites (M = Sc, Ti, V, Cr, Mn, Fe, Co, and Ni) to identify perovskites that exhibit simultaneous redox activity and are suitable for STCH (or STCC). Specifically, we evaluate the oxygen vacancy formation energy at 0 K ($E_f[Va_O] \approx \Delta H_{red}$), referenced to O_2 gas also at 0 K, the thermodynamic stability at 0 K, and the electronic structure (i.e., band gaps) for ternary $CaMO_3$, ternary $CeMO_3$, and quaternary $Ca_{0.5}Ce_{0.5}MO_3$ perovskites using density functional theory (DFT[47,48])-based calculations. Thus, the ternary perovskites considered have either Ca or Ce on the A site and a 3d transition metal on the B site, with the quaternary perovskites having an equal proportion of Ca and Ce mixed on the A site. We do not consider Cu and Zn atoms on the B site since both metals typically do not exhibit oxidation states higher than +2, which does not provide for the desired charge neutrality in a $Ca_{0.5}Ce_{0.5}MO_3$ or $CaMO_3$ framework.

A recent analysis[14] has suggested that a ΔH_{red} in the range of ∼3.4−3.9 eV is a good target range for improved STCH materials, where the ΔH_{red} is referenced to O_2 gas at a reduction temperature >1573 K. Typically, high (low) values of ΔH_{red} lead to a decrease (increase) in oxygen evolution in reducing conditions and increase (decrease) in water-splitting yield in oxidizing conditions. Given that DFT errors in defect formation energies are typically ±0.1 eV[49−51] and assuming that experimental optimization of composition and processing techniques can cause another ±0.1 eV deviation in ΔH_{red}, we use a range of 3.2−4.1 eV as a target window to evaluate potential candidates. Importantly, we find that $Ca_{0.5}Ce_{0.5}MnO_3$ and $Ca_{0.5}Ce_{0.5}FeO_3$ are promising candidates that exhibit an $E_f[Va_O]$ within the target window for STCH. Additionally, we present substantial evidence for simultaneous reduction of both Ce and Mn ions in $Ca_{0.5}Ce_{0.5}MnO_3$, thus leading to a perovskite structure that can exhibit simultaneous redox activity and an associated increased ΔS_{red} relative to ceria and other perovskites. In addition, we expect $Ca_{0.5}Ce_{0.5}VO_3$ to be a potential STCH candidate, where variations in the Ca−Ce configuration can bring the oxygen vacancy formation within the STCH-target range. We also discuss trends in the calculated vacancy formation energies and thermodynamic stabilities and offer insights useful for follow-up experimental and theoretical studies.

The structure of this paper is as follows. In section 2, we quantify the impact of simultaneous cation redox activity on the overall oxygen evolution capacity in a practical STCH process. In section 2.1, we identify potential structural, charge-neutrality, and redox-activity constraints that led us to the quaternary composition of $Ca_{0.5}Ce_{0.5}MO_3$. Sections 3 and 4 respectively detail the computational methods used in this work and the workflow of calculations (including schemes to generate theoretical structures). Section 5 contains our results, starting with the ternaries (section 5.1), then the quaternaries (section 5.2), followed by a discussion of the candidates identified (section 5.3). Section 6 outlines the role of some of the assumptions made and avenues for future research. Finally, section 7 offers concluding remarks.

2. IMPACT OF SIMULTANEOUS CATION REDOX

Figure 1a displays the configurational entropy of reduction (S_{config}) for a given perovskite (ABO_3), as a function of the oxygen concentration (x) in ABO_x. S_{config} is referenced with respect to the stoichiometric ABO_3, since there are no configurational degrees of freedom at the ABO_3 composition. In addition, we restrict ourselves to the configurational degree of freedom on the cation sublattices and ignore any electronic (entropy from metallic bands), vibrational (phonons), magnetic (spin alignments), and other degrees of freedom that may contribute to the overall ΔS_{red}. Scenarios shown include simultaneous cation reduction, i.e., both A and B reduce (solid red curve; two sublattices) and the case of only A or B being redox-active (dashed blue curve; one sublattice).

The mathematical expressions for S_{config} for both the one and two sublattice scenarios are given in eq 1, where k_B is the Boltzmann constant, x is the oxygen concentration, and δ is the oxygen off-stoichiometry. Specifically, $\delta = 3 - x$ in ABO_x and $\delta = 2 - x$ in CeO_x.

$$\begin{aligned}
&S_{config}(1\text{ sublattice, }ABO_{3-\delta})\\
&\quad = -k_B(2\delta\ln 2\delta + (1-2\delta)\ln(1-2\delta))\\
&S_{config}(2\text{ sublattices, }ABO_{3-\delta})\\
&\quad = -2k_B(\delta\ln\delta + (1-\delta)\ln(1-\delta))\\
&S_{config}(1\text{ sublattice, }ABO_x)\\
&\quad = -k_B((6-2x)\ln(6-2x) + (2x-5)\ln(2x-5))\\
&S_{config}(2\text{ sublattices, }ABO_x)\\
&\quad = -\,2k_B((3-x)\ln(3-x) + (x-2)\ln(x-2))
\end{aligned} \tag{1}$$

For the purposes of this simple analysis in Figure 1a and eq 1, we assume an ideal configurational entropy in both scenarios of cation reduction, i.e., the excess electrons arising from TR mix freely on the A and/or B sites. Additionally, for simultaneous redox, we assume that the two excess electrons arising from removing a neutral oxygen atom from the anion lattice distribute themselves equally on both A- and B-cation sites, i.e., both A and B reduce to the same extent. Furthermore, we restrict the range of our calculations to $2.5 \leq x \leq 3$, where the lowest value of x (2.5, equivalent to $ABO_{2.5}$) represents an oxygen off-stoichiometry of 0.5 mol of O/f.u., which corresponds to an addition of 1 mole of electrons. Thus, in a one sublattice scenario, a composition of $ABO_{2.5}$ corresponds to either all A or all B sites being reduced (similar to all Ce atoms being reduced in $CeO_{1.5}$). Importantly, simultaneous cation reduction always leads to a higher S_{config} than a single cation reduction, as indicated by the red curve being strictly more positive than the dashed blue curve across all x in Figure 1a, consistent with the fact that simultaneous cation reduction provides more configurational degrees of freedom. Moreover, while S_{config} maximizes for a single cation reduction at $x = 2.75$ (off-stoichiometry of 0.25; equivalent to the addition of 0.5 mol of electrons), the maximum occurs at $x = 2.5$ for simultaneous cation reduction (off-stoichiometry of 0.5; addition of 1 mole of electrons).

To quantify further the role of S_{config} in determining the equilibrium oxygen off-stoichiometry (i.e., $\delta_{eq} = 3 - x_{eq}$ in ABO_x and $\delta_{eq} = 2 - x_{eq}$ in CeO_x), we plot the derivative of the configurational entropy with respect to the oxygen off-stoichiometry in Figure 1b. In contrast to Figure 1a, we include the contribution of configurational entropy in both the cation and anion sublattices in Figure 1b. Note that for a given temperature (T) and oxygen partial pressure (p_{O_2}), δ_{eq} is determined by the oxygen chemical potential (μ_O) within the $ABO_{3-\delta}$ perovskite. Specifically, δ_{eq} is the δ at which $\mu_O = \mu_O^{O_2(g)}$, where $\mu_O^{O_2(g)}$ is the oxygen chemical potential of oxygen gas and equals half the Gibbs energy of O_2 gas. μ_O is the derivative of the Gibbs energy of $ABO_{3-\delta}$ with respect to oxygen concentration, i.e.,

$$\mu_O = \frac{dG_{ABO_x}}{dx} = -\frac{dG_{ABO_{3-\delta}}}{d\delta}$$

For a given temperature, oxygen partial pressure, and $[dH_{ABO_{3-\delta}}]/[d\delta]$, μ_O is linearly dependent on $[dS_{ABO_{3-\delta}}]/[d\delta]$. Hence, the derivative of the entropy determines any variation in δ_{eq}, at a given reduction enthalpy (and given T, p_{O_2}).

We plot the derivative of the configurational entropy as a function of the normalized off-stoichiometry (δ/n) in Figure 1b, where n is the number of atoms in the stoichiometric oxide ($n = 3$ in CeO_2 and 5 in ABO_3). We provide the necessary mathematical expressions for ${}^{dS_{config}}/_{d\delta}$ in single reduction perovskites (dashed blue line), simultaneous reduction perovskites (solid red line), and $CeO_{2-\delta}$ (solid orange line) in eq 2.

$$\begin{aligned}
&\frac{dS_{config}}{d\delta}(1\text{ sublattice, }ABO_{3-\delta})\\
&\quad = -k_B\left[2\ln\left(\frac{2\delta}{1-2\delta}\right) + \ln\left(\frac{\delta}{3-\delta}\right)\right]\\
&\frac{dS_{config}}{d\delta}(2\text{ sublattices, }ABO_{3-\delta})\\
&\quad = -k_B\left[2\ln\left(\frac{\delta}{1-\delta}\right) + \ln\left(\frac{\delta}{3-\delta}\right)\right]\\
&\frac{dS_{config}}{d\delta}(CeO_{2-\delta}) = -k_B\left[2\ln\left(\frac{2\delta}{1-2\delta}\right) + \ln\left(\frac{\delta}{2-\delta}\right)\right]
\end{aligned} \tag{2}$$

We chose $CeO_{2-\delta}$ for comparison as it is the state-of-the-art material for STCH.[5,14] Importantly, ${}^{dS_{config}}/_{d\delta}$ for a simultaneous cation redox remains positive and is always higher than $CeO_{2-\delta}$ throughout the range of δ/n considered. In the case of a single cation redox, ${}^{dS_{config}}/_{d\delta}$ is strictly lower than both simultaneous redox and $CeO_{2-\delta}$ for all δ/n. Overall, the shape of the ${}^{dS_{config}}/_{d\delta}$ curve primarily dictates the evolution of μ_O within the solid, as a function of δ or δ/n.

We then provide an estimate of the δ_{eq}, at $T = 1673$ K and $p_{O_2} = 10^{-4}$ atm (relevant for STC TR[5]), in a single redox-active sublattice perovskite (blue lines and text), a simultaneous two redox-active sublattice perovskite (red lines and text), and

$CeO_{2-\delta}$ (orange lines and text) in Figure 1c. To obtain δ_{eq}, we use a modified regular solution model to describe the underlying Gibbs energy (G) of the solid (relevant expressions in eq 3) and subsequently take the derivative with respect to δ to obtain μ_O.

$$\begin{aligned} G_{ABO_{3-\delta}} = {} & (1-2\delta)G_{ABO_3} + 2\delta G_{ABO_{2.5}} + L_0\delta \\ & - TS_{\text{config}}(\delta) + 3k_BT\left(\frac{\delta}{3}\ln\frac{\delta}{3} + \left(1-\frac{\delta}{3}\right)\right. \\ & \left.\ln\left(1-\frac{\delta}{3}\right)\right) \\ G_{CeO_{2-\delta}} = {} & (1-2\delta)G_{CeO_2} + 2\delta G_{CeO_{1.5}} + L_0\delta \\ & + k_BT[(2\delta\ln 2\delta + (1-2\delta)\ln(1-2\delta)] \\ & + 2k_BT\left[\frac{\delta}{2}\ln\frac{\delta}{2} + \left(1-\frac{\delta}{2}\right)\ln\left(1-\frac{\delta}{2}\right)\right] \end{aligned} \tag{3}$$

G_{ABO_3} and $G_{ABO_{2.5}}$ in eq 3 are the Gibbs energies of hypothetical pristine ABO_3 and defective $ABO_{2.5}$ perovskite phases, which are set to the calculated Gibbs energies of CeO_2 (G_{CeO_2}) and $CeO_{1.5}$ ($G_{CeO_{1.5}}$) in the fluorite structure.[52] Additionally, we set the enthalpy to form an oxygen vacancy (or the enthalpy of mixing oxygen vacancies with oxygen atoms; L_0 term in eq 3) to a constant value across all x, where the value used is identical to the DFT-calculated $E_f[Va_O]$ in $CeO_{2-\delta}$ at $\delta \to 0$ (= 3.98 eV/Va_O).[43,52,53] These approximations ensure that we capture the effect of entropy, while fixing ΔH_{red}, T, and p_{O_2}. The prefactors of $(1 - 2\delta)$ and (2δ) that multiply with G_{CeO_2} (or G_{ABO_3}) and $G_{CeO_{1.5}}$ (or $G_{ABO_{2.5}}$), respectively, normalize the Gibbs energy contributions of these phases in accordance with the lever rule of thermodynamics. The final additive terms on the right-hand side of the expressions for $G_{ABO_{3-\delta}}$ and $G_{CeO_{2-\delta}}$ in eq 3 are the configurational entropy terms on the cation and oxygen sublattices due to vacancy formation (S_{config} (δ) is identical to eq 1). The numerical prefactors of 3 and 2 that multiply the anion sublattice configurational entropy terms reflect the number of oxygen atoms in stoichiometric ABO_3 and CeO_2, respectively. Note that $\delta/3$ and $\delta/2$ within the oxygen sublattice entropy terms indicate the fraction of Va_O in the oxygen sublattices of $ABO_{3-\delta}$ and $CeO_{2-\delta}$, respectively, with the conjugate terms (i.e., $1 - \delta/3$ and $1 - \delta/2$) signifying the fraction of oxygen atoms. The dash-dotted green line corresponds to $\mu_O^{O_2(g)}$ at T = 1673 K and a $p_{O_2} = 10^{-4}$ atm, obtained from experimental data.[54] The zero of μ_O, conventionally set to the highest chemical potential that the element can reach, is set here to the total energy of O_2 gas at 0 K, as calculated with DFT (see section 3); for reference, $\mu_O^{O_2(g)}$ (298 K, 1 atm) = −0.31 eV.[54]

Importantly, this simple analysis predicts that the equilibrium off-stoichiometry with simultaneous cation reduction in a perovskite is higher (~0.014 mol of O/n or 0.069 mol of O/f.u.) compared to single cation redox in ABO_3 (~0.009 mol of O/n or 0.043 mol of O/f.u.) and $CeO_{2-\delta}$ (~0.013 mol of O/n or 0.038 mol of O/f.u.). In other words, simultaneous redox activity could yield a normalized oxygen evolution capacity that is respectively ~60% and 9% higher than the single-sublattice scenario and $CeO_{2-\delta}$ at 1673 K, $p_{O_2} = 10^{-4}$ atm, and ~4 eV reduction enthalpy. The 60% and 9% excess normalized capacity in the two-sublattice perovskite is similar for other temperatures (1573−1773 K) and p_{O_2} (10^{-5} to 10^{-3} atm) conditions. Note that the modified regular solution model used here overestimates the oxygen evolution capacity of $CeO_{2-\delta}$; experiments have reported a capacity of 0.005 mol of O/n or ~0.014 mol of O/f.u. due to the observed higher reduction enthalpy (>4 eV) and its variation with δ.[42] Nevertheless, for any combination of temperature, p_{O_2}, and enthalpy of reduction, simultaneous cation reduction always leads to a higher reduction extent during the TR step. A higher reduction extent in turn produces larger quantities of hydrogen during the WS step per unit of redox active material, thus improving the overall efficiency of a STCH cycle, assuming less than perfect heat recovery between the reduction and reoxidation steps.

2.1. Composition Selection. Three major constraints limit the number of possible compositions that can exhibit simultaneous cation reduction in a perovskite framework, namely, structural, charge neutrality, and redox activity. For example, the ABO_3 perovskite framework typically has an A atom that is significantly (>15%) larger than the B atom (typically a 3d metal), which limits the possible (A,B) combinations that can exist in nature.[55,56] Additionally, there are five possible combinations of (A,B) oxidation states that can exist ensuring charge neutrality of the ABO_3 framework: (+1,+5), (+2,+4), (+3,+3), (+4,+2), and (+5,+1). Among the possible (A,B) oxidation state combinations, (+1,+5) and (+5, +1) are not relevant because cations, if reduced from a +1 state to 0, will no longer be bound within the ABO_3 framework, i.e., reducing a +1 cation to its metallic state will destabilize the perovskite structure. Similarly, A cations that usually exhibit a +2 oxidation state (e.g., alkaline-earth metals) do not undergo reduction to a +1 oxidation state, ruling out a (+2,+4) combination. Hence, the combination of charge neutrality and redox activity yields (+3,+3) and (+4,+2) as the only possible (A,B) combinations that can be simultaneously redox-active.

Among large metal (alkali, alkaline-earth, rare-earth, p-block) elements that can exhibit either a +3 or a +4 oxidation state, most of the elements are either toxic (e.g., Pb^{4+}, which can reduce to Pb^{2+}) and/or rare (lanthanides beyond Ce). Hence, Ce is the only realistic option that exhibits both a +3 and a +4 oxidation state and is also redox-active, i.e., $Ce^{4+} \to Ce^{3+}$ is a feasible reduction process. If Ce were to completely occupy the A site, the resulting ABO_3 perovskite has both (+3, +3) and (+4,+2) oxidation state combinations possible. However, both combinations cannot sustain simultaneous redox activity. For example, in the (A,B) = (+3,+3) combination, Ce^{3+} is not redox-active. Similarly, in the (+4, +2) combination, all 3d metals (except Cu) are not redox-active, i.e., do not exhibit a $M^{2+} \to M^{+}$ reduction, leaving Ce^{4+} to be the only redox-active component. Note that we do not consider $CeCuO_3$ in our calculations due to limitations in the theoretical description of $Cu^{2+} \to Cu^{+}$ reduction in oxides.[57]

To ensure that both Ce and the 3d metal remain redox-active, we need to target a quaternary $(A,A')BO_3$ composition such that the overall oxidation state of A+A′ = 3, with Ce in its +4 oxidation state. We chose Ca as the additional element to go on the A site apart from Ce because of its nominal oxidation state (+2) and similarity in size, as indicated by the ionic radius[58] of Ca^{2+} (1.18−1.34 Å for coordination numbers 8−12) and Ce^{4+} (0.97−1.14 Å). Further, to ensure that the oxidation state of A + A′ = 3, we chose a 1:1 Ca:Ce proportion within the perovskite structure, resulting in a $Ca_{0.5}Ce_{0.5}MO_3$ composition. Moreover, there is experimental evidence for the mixing of Ca and Ce leading to formation of a (Ca,Ce)MnO_3 perovskite,[59,60] suggesting that other (Ca,Ce)MO_3 compositions may be feasible experimentally.

Since $Ti^{4+} \rightarrow Ti^{3+}$ reduction is more common in oxides than a $Ti^{3+} \rightarrow Ti^{2+}$ reduction, we considered a quinary extension of the $Ca_{0.5}Ce_{0.5}TiO_3$, namely, $Ca_{0.5}Ce_{0.5}Ti_{0.5}Mg_{0.5}O_3$, where the choice of Mg^{2+} is also because of its similar ionic radius to Ti^{4+}.[58] Although quaternary $Ca_{0.5}Ce_{0.5}MO_3$ perovskites are the primary candidates for simultaneous cation redox, we evaluated the ternary $CaMO_3$ and $CeMO_3$ perovskites as well for consistency and completeness. Although ternary oxide perovskites have been theoretically screened as candidates before,[31,34] we use a SCAN+U framework along with a more diverse set of space groups as template structures (see Section 4) to obtain useful trends and descriptors. Note that quaternary $Ca_{0.5}Ce_{0.5}MO_3$ perovskites where M = a 4d or 5d metal are also (theoretically) possible but are left for future work.

3. COMPUTATIONAL METHODS

We used the Vienna ab initio simulation package (VASP)[61,62] to perform spin-polarized DFT+U calculations using with the projector augmented-wave potentials[63] we employed previously.[57,64] We used the Hubbard U[65,66] corrected strongly constrained and appropriately normed[67] (i.e., SCAN+U[64]) functional to describe electron exchange and correlation, with U values determined in prior work.[57,64] The U correction was applied to all 3d and 4f metal orbitals, with the exception of Sc and Cr.[57] We used a kinetic energy cutoff of 520 eV for the planewave basis, employed Gaussian smearing (width = 0.05 eV) to integrate over the Fermi surface, and sampled the Brillouin zone of each structure with a dense, Γ-point-centered, Monkhorst–Pack[68] k-point mesh (spacing ≤ 0.025 Å^{-1}), consistent with our previous studies.[57,64] The total energies and atomic forces were converged to 0.01 meV/cell and $< |0.05|$ eV/Å, respectively. The magnetic moments of all 3d ions were aligned ferromagnetically in all calculations for simplicity in the screening process. Moreover, previous computational studies[31,69] have reported that using a ferromagnetic versus antiferromagnetic configuration to model the bulk perovskite changes the $E_F[Va_O]$ by ±0.1 eV, which is within the range of our target window (3.2−4.1 eV). In the case of bulk structural relaxation for ternary perovskites, we did not preserve symmetry for structures that are originally from the inorganic crystal structure database (ICSD[70]), and we allowed the cell volume, cell shape, and ion coordinates to change (i.e., all structural degrees of freedom allowed to relax). However, for theory-derived structures (see below), we first perform a bulk structural relaxation preserving space group symmetry followed by a relaxation of the ionic positions alone without preserving symmetry. We adopted this procedure to avoid any large-scale structural distortion and to ensure that we can clearly identify which theoretical structure is the lowest energy polymorph among those considered at a given composition. In the case of bulk structural relaxation of quaternary perovskites, we did not preserve the symmetry and allowed all degrees of freedom to relax. All band gaps reported here are from electron density of states (DOS) calculations, in which we evaluate the DOS at energy intervals of 0.005 eV.

We performed only neutral defect calculations to model Va_O formation, i.e., we remove both the oxygen nucleus and all of its electrons that comprise the atom to create an oxygen vacancy. The Va_O formation energy is given by eq 4, where $E^{SCAN+U}_{defective}$, $E^{SCAN+U}_{pristine}$, and $E^{SCAN}_{O_2(g)}$ are the total energies of the defective perovskite, pristine perovskite, and oxygen gas, respectively, with the superscripts on the E terms indicating the level of theory used.

$$E_F[Va_O] = E^{SCAN+U}_{defective} - E^{SCAN+U}_{pristine} + \frac{1}{2}E^{SCAN}_{O_2(g)} \quad (4)$$

For all Va_O calculations, we used supercells with a minimum of 10 Å lattice spacing between vacancies in all directions to minimize interactions of the defect with its periodic image, leading to a $E_F[Va_O]$ that is converged to within ±0.1 eV. Additionally, we relax only the ionic positions of defective structures (i.e., with Va_O) while fixing the lattice parameters to that of the corresponding pristine bulk.

To evaluate the 0 K thermodynamic stability, we obtain all elements, binary Ca−O, Ce−O, and M−O; ternary Ca−Ce−O, Ca−M−O, and Ce−M−O; and quaternary Ca−Ce−M−O structures that are available within the ICSD and calculate their total energies within our SCAN+U framework. While we obtained the total energy of O_2 (i.e., $E_{O_2(g)}$, eq 4) from our prior work,[64] all other elemental structures were calculated with DFT-SCAN, i.e., without any U corrections, as the optimal physical model of pure metals. Although mixing DFT-SCAN and SCAN+U total energies is inconsistent, such mixing only affects regions of the phase diagram that are M-rich, which is far away from the region of existence of the perovskites considered in this work. Hence, the 0 K thermodynamic stabilities reported here are obtained from a consistent treatment of all competing structures at the same theoretical level. Note that we only included ICSD structures that are "ordered," i.e., all sites in a given structure have integer atomic occupations. After calculating the total energies using SCAN+U/DFT-SCAN, we used the pymatgen[71] package to construct the 0 K phase diagrams.

4. WORKFLOW AND STRUCTURE SELECTION

To systematically evaluate the $E_F[Va_O]$ of ternary $CaMO_3$, $CeMO_3$, and quaternary $Ca_{0.5}Ce_{0.5}MO_3$ perovskites considered here, we developed the workflow illustrated in Figure 2. All green boxes in Figure 2 signify SCAN+U calculations, while the blue boxes indicate postprocessing steps to obtain theoretical structures for calculations. Although there are several $CaMO_3$ and $CeMO_3$ ternary structures available in the ICSD, there are no ordered quaternary $Ca_{0.5}Ce_{0.5}MO_3$ structures available. Hence, all quaternary perovskite structures considered here are theoretical. We list all ternary and quaternary perovskites studied in this work in Table 1 along with their origin (ICSD/theoretical for ternaries, original ternary perovskite structure for the quaternaries), space group, oxidation state of the cations, band gap from DOS calculations, and the redox-active species (upon Va_O formation). The basis for the oxidation state of each cation in the pristine materials listed in Table 1 is the on-site magnetic moment(s) as

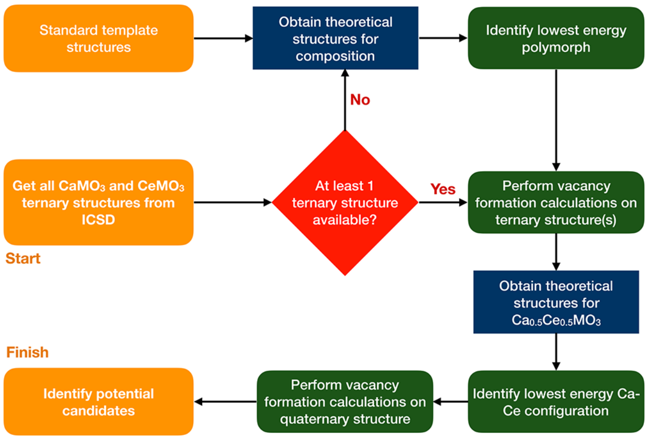

Figure 2. Workflow for calculating oxygen vacancy formation energies in ternary and quaternary perovskites considered in this work.

Table 1. All Ternary and Quaternary Perovskites Considered in This Work along with the Origin of the Structure, Space Group, Oxidation States of Cations, Band Gap, and Redox-Active Species[a]

composition	origin of structure	space group	oxidation state Ca	oxidation state Ce	oxidation state M	band gap (eV)	redox-active species
			ternaries				
$CaScO_3$							
$CeScO_3$	ICSD	*Pnma*		+3	+3	1.45	Ce^{3+}
$CaTiO_3$	ICSD	*Pnma*	+2		+4	2.66	Ti^{4+}
$CeTiO_3$							
$CaVO_3$	ICSD	*Pnma*	+2		+4	0.25	V^{4+}
$CeVO_3$	ICSD	$P2/n$		+3	+3	metallic	V^{3+}
$CaCrO_3$	ICSD	*Pnma*	+2		+4	metallic	Cr^{4+}
$CeCrO_3$	ICSD	$Pm\bar{3}m$		+3	+3	0.34	Cr^{3+}
$CaMnO_3$	ICSD	*Pnma*	+2		+4	0.76	Mn^{4+}
$CeMnO_3$							
$CaFeO_3$	ICSD	$P2/n$	+2		+4	metallic	Fe^{4+}
$CeFeO_3$							
$CaCoO_3$	theory	$P2/b$	+2		+4	0.17	Co^{4+}
$CeCoO_3$	theory	*Pnma*		+4	+2	0.15	Ce^{4+}
$CaNiO_3$	theory	$P63/mmc$	+2		+4	1.43	Ni^{4+}
$CeNiO_3$	theory	$P2/b$		+4	+2	0.22	Ce^{4+}
			quaternaries				
$Ca_{0.5}Ce_{0.5}ScO_3$	$CeScO_3$	*Pnma*-based	+2	+4	+3	1.58	Ce^{4+}
$Ca_{0.5}Ce_{0.5}TiO_3$	$CaTiO_3$	*Pnma*-based	+2	+3	+4, +3	0.31	Ti^{4+}
$Ca_{0.5}Ce_{0.5}VO_3$	$CaVO_3$	*Pnma*-based	+2	+3	+4, +3	metallic	V^{4+}
	$CeVO_3$	$P2/n$-based	+2	+3	+4, +3	metallic	V^{4+}
$Ca_{0.5}Ce_{0.5}CrO_3$	$CaCrO_3$	*Pnma*-based	+2	+4	+3	0.02	Ce^{4+}
	$CeCrO_3$	$Pm\bar{3}m$-based	+2	+4	+3	0.03	Ce^{4+}
$Ca_{0.5}Ce_{0.5}MnO_3$	$CaMnO_3$	*Pnma*-based	+2	+4	+3	metallic	Ce^{4+}/Mn^{3+}
$Ca_{0.5}Ce_{0.5}FeO_3$	$CaFeO_3$	$P2/n$-based	+2	+4	+3	0.29	Ce^{4+}
$Ca_{0.5}Ce_{0.5}CoO_3$	$CaCoO_3$	$P2/b$-based	+2	+4	+3	1.24	Co^{3+}
	$CeCoO_3$	*Pnma*-based	+2	+4	+3	1.25	Co^{3+}
$Ca_{0.5}Ce_{0.5}NiO_3$	$CaNiO_3$	$P63/mmc$-based	+2	+3	+4, +3	0.25	Ni^{4+}
	$CeNiO_3$	$P2/b$-based	+2	+4	+4, +2	metallic	Ni^{4+}

[a] While ternary perovskites originate either from the ICSD or from theory, all quaternary perovskites are theoretical structures derived from one of the ternaries. Oxidation states in the pristine material are deduced from SCAN+*U* on-site magnetic moments. Band gaps in the pristine material are estimated from SCAN+*U* DOS. Redox-active species in the pristine material are identified by changes in local electronic structure upon removal of a neutral oxygen atom.

calculated by VASP. In the case of defective structures, we identify the redox-active cation from on-site magnetic moment(s) and/or DOS calculations. Figure S1 of the Supporting Information (SI) displays the lowest energy Ca–Ce configurations of all quaternary perovskites.

To begin the workflow, we search for and obtain ICSD structures for ternary $CaMO_3$ and $CeMO_3$ perovskites. If only one ICSD structure exists for $CaMO_3$ or $CeMO_3$, we perform all subsequent calculations using that structure. For example, among $CaScO_3$ and $CeScO_3$, an ICSD structure is only available for $CeScO_3$. Hence, we use the $CeScO_3$ as the base for obtaining quaternary $Ca_{0.5}Ce_{0.5}ScO_3$ configurations. This follows experimental synthetic intuition, whereby one first produces a known structure (with a known synthesis procedure) followed by substitution of some of the Ce ions with Ca. If new experimental procedures (and/or precursors) are proposed and used to obtain the $Ca_{0.5}Ce_{0.5}ScO_3$ perovskite, it is typically easier to use variants from those used to produce $CeScO_3$. In the cases where there is an ICSD structure for each $CaMO_3$ and $CeMO_3$ (such as for $CaCrO_3$ and $CeCrO_3$), we consider both structures in all subsequent calculations. If multiple ICSD structures exist for a given composition (e.g., $CeVO_3$), we perform all subsequent calculations only with the lowest energy polymorph. In the absence of any ICSD entry, as is the case for $CaCoO_3$, $CeCoO_3$, $CaNiO_3$, and $CeNiO_3$, we use "template" structures (see Figure 3 and text below) to obtain a set of theoretical structures exhibiting different perovskite space groups. Subsequently, we use SCAN+*U* calculations to evaluate the lowest energy polymorph for each composition, and we use that polymorph for all subsequent calculations. We consider both possible ternary perovskites for Co (i.e., $CaCoO_3$ and $CeCoO_3$) and for Ni ($CaNiO_3$ and $CeNiO_3$) since we do not know *a priori* which ternary perovskite will be feasible to synthesize.

Once we obtain a set of lowest-energy, ICSD/theoretical $CaMO_3$ and $CeMO_3$ structures, we calculate the $E_F[Va_O]$ within the ternary perovskite(s). Next, we use pymatgen[71] to obtain all possible symmetrically distinct configurations of $Ca_{0.5}Ce_{0.5}MO_3$ (i.e., distinct Ca+Ce configurations) within each ternary perovskite unit cell considered (except $CeCrO_3$). Subsequently, we use SCAN+*U* calculations to identify the lowest energy quaternary configuration. For $CeCrO_3$, we use a $2 \times 2 \times 2$ supercell since the unit cell has a single A site. We do not consider possible Ca–Ce configurations in larger supercells to keep the computational expenses tractable. In the cases where multiple ternary perovskites are considered (e.g., $CaVO_3$

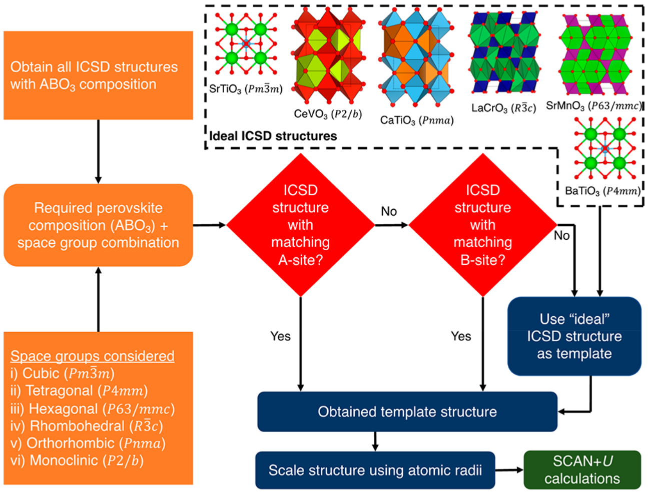

Figure 3. Scheme to obtain theoretical structures for ternary Co and Ni perovskites, namely, $CaCoO_3$, $CeCoO_3$, $CaNiO_3$, and $CeNiO_3$.

and $CeVO_3$), we obtain the lowest-energy $Ca_{0.5}Ce_{0.5}MO_3$ configuration from both ternaries. Throughout the rest of the paper, we indicate $Ca_{0.5}Ce_{0.5}MO_3$ obtained from a $CaMO_3$ ($CeMO_3$) perovskite as “$CaMO_3$-based” (“$CeMO_3$-based”). Finally, we calculate the $E_F[Va_O]$ in the lowest-energy quaternary $Ca_{0.5}Ce_{0.5}MO_3$ configuration, as obtained from all relevant ternary perovskites, and identify candidates for STCH or STCC applications. For both ternary and quaternary perovskites, we calculate the formation energy for all symmetrically distinct configurations of Va_O within the corresponding supercell structures. Furthermore, for each ternary and quaternary perovskite considered, we evaluate the 0 K thermodynamic stability. Wherever possible, we also calculate the DOS of ternary and quaternary perovskites with a Va_O. With respect to quinary $Ca_{0.5}Ce_{0.5}Ti_{0.5}Mg_{0.5}O_3$, we used the $CaTiO_3$ *Pnma* ICSD structure as the base, substituted half the Ca and Ti sites with Ce and Mg, respectively, and used the lowest-energy quinary configuration to calculate $E_F[Va_O]$.

Figure 3 displays the templating scheme that we used for generating theoretical structures, specifically $CaCoO_3$, $CeCoO_3$, $CaNiO_3$, and $CeNiO_3$. For each composition, we considered a set of six possible perovskite space groups, namely, cubic ($Pm\bar{3}m$), tetragonal ($P4mm$), hexagonal ($P63/mmc$), rhombohedral ($R\bar{3}c$), orthorhombic ($Pnma$), and monoclinic ($P2/b$ or $P2/c$). In parallel, we acquired all ABO_3 perovskite structures from the ICSD. Given a combination of a composition (e.g., $CaCoO_3$) and a space group (e.g., $Pm\bar{3}m$), we first check the ICSD for $CaBO_3$ ($B \neq Co$) perovskites in the $Pm\bar{3}m$ space group, i.e., perovskite structures with a matching A site, to be used as a template. We search for matching A-site structures since the A cation is typically the largest ion within the perovskite framework. If there are no matching $CaBO_3$ structures, we search for $ACoO_3$ ($A \neq Ca$) structures in the $Pm\bar{3}m$ space group, i.e., matching the B site. In the absence of either $CaBO_3$ or $ACoO_3$ structures in the desired space group, we use a set of “ideal” perovskite structures from the ICSD to act as the template, as highlighted by the structures included in the dashed black box in Figure 3. Specifically, we use $SrTiO_3$ ($Pm\bar{3}m$), $BaTiO_3$ ($P4mm$), $SrMnO_3$ ($P63/mmc$), $LaCrO_3$ ($R\bar{3}c$), $CaTiO_3$ ($Pnma$), and $CeVO_3$ ($P2/b$) as our ideal perovskites. We chose all the ideal structures to maximize the diversity of A and B cations with the constraint that there are experimental structures available within the desired space group.

Having identified the matching template structure, we obtain the desired theoretical structure by substituting the existing species (e.g., B in $CaBO_3$) with the desired species (e.g., Co). Additionally, we scale the lattice vectors of the desired composition (say $A'B'O_3$) from the template composition (say $A''B''O_3$) according to the ratio of atomic radii[72] of the species involved, as indicated by eq 5,[73] where V indicates the lattice volume and r_j is the atomic radius of species j.

$$V^{\text{desired}} = V^{\text{template}}\left(\frac{r_{A'} + r_{B'} + \sqrt[3]{3}\,r_O}{r_{A''} + r_{B''} + \sqrt[3]{3}\,r_O}\right)^3 \qquad (5)$$

The specific lattice vectors are calculated after obtaining the scaled volume by preserving the ratios of the lattice vectors ($a{:}b$ and $a{:}c$) of the template structure. The prefactor of $\sqrt[3]{3}$ before r_O reflects three oxygen atoms in both the desired and template structures. Our templating scheme (Figure 3) is quite general and easily extended to any desired perovskite + space group combinations for applications other than STCH. Finally, we perform SCAN+U calculations on the theoretical structures obtained, according to the workflow presented in Figure 2.

5. RESULTS

First, we present results relevant for ternary $CaMO_3$ and $CeMO_3$ systems followed by quaternary $Ca_{0.5}Ce_{0.5}MO_3$ systems, following the workflow of Figure 2 to show evidence that simultaneous redox is possible. Specifically, we discuss predicted ground-state polymorphs for Co and Ni perovskites, followed by the $E_F[Va_O]$ and thermodynamic stabilities of all ternary perovskites and analyze important trends in section 5.1. Subsequently, we present the $E_F[Va_O]$ and thermodynamic stabilities of quaternary perovskites in section 5.2 and focus on potential candidates based on simultaneous redox and suitable reduction enthalpies in section 5.3.

5.1. Ternary CaMO3 and CeMO3 Perovskites.

5.1.1. Ground-State Polymorphs for Co and Ni Perovskites. Figure 4 presents total energies of the theoretical Co and Ni perovskite polymorphs relative to the corresponding lowest-energy (or ground state, GS) polymorph at each composition, which are indicated by the black arrows. Note that the energy scale in Figure 4 truncates at 0.2 eV/f.u., with several polymorphs exhibiting energy differences higher than 0.2 eV/f.u. above the corresponding E_{GS}. Figure 4 also depicts the

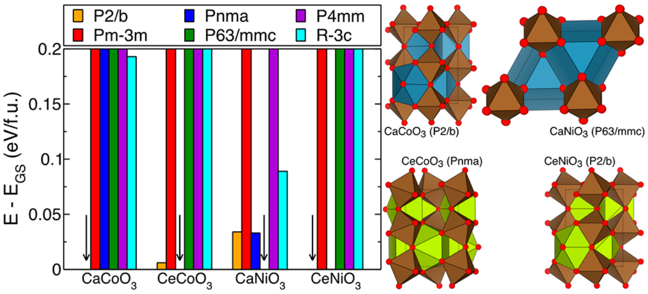

Figure 4. Energies of various theoretical polymorphs plotted with respect to their corresponding ground-state configuration (indicated by black arrows) for $CaCoO_3$, $CeCoO_3$, $CaNiO_3$, and $CeNiO_3$. The structures displayed (along with the space group) reflect the ground-state polymorph at each composition.

lowest-energy polymorph at each composition, namely, $CaCoO_3$ (*P*2/*b*, monoclinic), $CaNiO_3$ (*P*63/*mmc*, hexagonal), $CeCoO_3$ (*Pnma*, orthorhombic), and $CeNiO_3$ (*P*2/*b*), where blue, yellow, and brown polyhedra indicate Ca, Ce, and Co/Ni atoms, respectively. Among the GSs generated, $CaCoO_3$ (*P*2/*b*), $CeCoO_3$ (*Pnma*), and $CeNiO_3$ (*P*2/*b*) originate from A-site matching (see Figure 3), while $CaNiO_3$ (*P*63/*mmc*) results from B-site matching.

Among the metastable configurations, $CaCoO_3$ ($Pm\bar{3}m$, *Pnma*), $CeCoO_3$ (*P*2/*b*, $Pm\bar{3}m$), $CaNiO_3$ ($Pm\bar{3}m$, *P*2/*b*, *Pnma*), and $CeNiO_3$ ($Pm\bar{3}m$, *Pnma*) are the A-site matched configurations, while $CaCoO_3$ (*P*63/*mmc*, $R\bar{3}c$), $CeCoO_3$ (*P*63/*mmc*, $R\bar{3}c$), $CaNiO_3$ ($R\bar{3}c$), and $CeNiO_3$ (*P*63/*mmc*, $R\bar{3}c$) are B-site matched polymorphs. Interestingly, all *P*4*mm* polymorphs are ideal-structure-matched configurations exhibiting high energies above the GS (>0.2 eV/f.u.), signifying inaccessibility in experiments and unsuitability. From this point onward, all references to $CaCoO_3$, $CaNiO_3$, $CeCoO_3$, and $CeNiO_3$ reflect their corresponding GS configurations. In the case of $CeNiO_3$, the *Pnma* polymorph is quite close in energy compared to the *P*2/*b*, at 0.07 meV/f.u. The *Pnma* and *P*2/*b* polymorphs are similar in terms of cation configuration, with the primary difference being that the lattice vectors in *P*2/*b* are nonorthogonal, while those of *Pnma* are orthogonal. Although the *Pnma* and *P*2/*b* polymorphs are nearly degenerate in energy, we perform all subsequent calculations on $CeNiO_3$ only with the *P*2/*b* polymorph to reduce computational costs. Among Co perovskites, $CeCoO_3$ *Pnma* and *P*2/*b* structures differ in energy by only ∼6 meV/f.u., while the analogous energy difference in $CaCoO_3$ is quite drastic (∼337 meV/f.u.), highlighting the role of the A cation in the stability of a given ABO_3 perovskite framework.

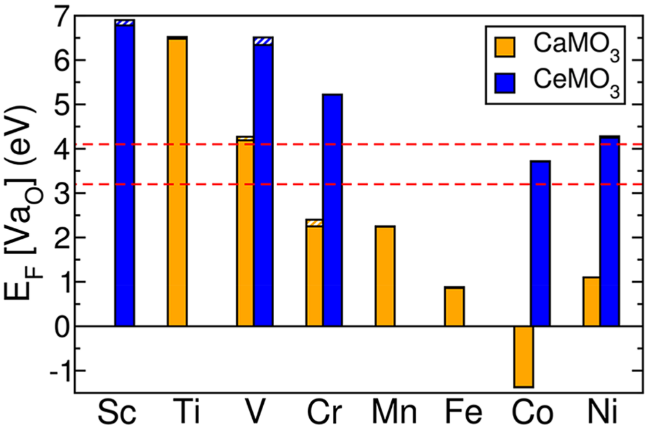

Figure 5. Oxygen vacancy formation energy in all $CaMO_3$ (orange bars) and $CeMO_3$ (blue bars) considered in this work. Dashed red lines indicate the target range for solar thermochemical hydrogen generation (3.2−4.1 eV). Hashed region on each bar is the variability of vacancy formation energy due to symmetrically distinct oxygen vacancy configurations.

5.1.2. Oxygen Vacancy Formation Energy. Figure 5 displays oxygen vacancy formation energies of all ternary perovskites considered here. Orange (blue) bars indicate $CaMO_3$ ($CeMO_3$) structures, with the rationale for which $CaMO_3$ and/or $CeMO_3$ ternaries are studied already explained in section 4. The hashed region on a given bar signifies the variation in $E_F[Va_O]$ due to symmetrically distinct Va_O configurations within that structure. Dashed red lines indicate the window of $E_F[Va_O]$, i.e., 3.2−4.1 eV, that we consider the target for STCH applications (see Section 1). The $E_F[Va_O]$ in Figure 5 display a monotonically decreasing trend, in both $CaMO_3$ and $CeMO_3$ perovskites, as M progresses from Sc to Co, with Ni perovskites a notable exception. Thus, $CaCoO_3$ and $CeCoO_3$ exhibit the lowest $E_F[Va_O]$ within the $CaMO_3$ and $CeMO_3$ series, respectively. The negative value of $E_F[Va_O]$ in $CaCoO_3$ indicates that the bulk perovskite structure is likely unstable. Since a high-pressure cubic phase of $CaCoO_3$ has been reported experimentally,[74] we calculated the $E_F[Va_O]$ in the cubic structure as well and found it to be qualitatively similar (∼ −1.05 eV in cubic) to the *P*2/*b* structure (∼ −1.36 eV), further reinforcing the instability of a bulk $CaCoO_3$ phase. Importantly, $CeCoO_3$ (3.68 eV) is the only ternary perovskite whose $E_F[Va_O]$ falls within the target window for STCH, with $CaVO_3$ (4.18−4.27 eV) and $CeNiO_3$ (4.25−4.28 eV) being marginally beyond the target window. However, the technical viability of $CeCoO_3$ will depend on its thermodynamic stability (see section 5.1.3) and its eventual synthesizability. Additionally, there are other considerations, which might eliminate Co as a candidate, such as availability and security of supply.

Although structural, electrostatic (repulsion between cations), thermodynamic (stability), electronic (band gap), and chemical bonding (covalency versus ionicity) properties play a role in determining $E_F[Va_O]$, the monotonically decreasing $E_F[Va_O]$ trend in $CaMO_3$ perovskites bears a strong (anti)-correlation with the standard reduction potentials[75] of the redox-active element, namely, the M atom. For example, the standard reduction potentials vary (versus standard hydrogen electrode, SHE) as 0.19 V ($Ti^{4+} \rightarrow Ti^{3+}$) < 0.34 V ($V^{4+} \rightarrow V^{3+}$) < 0.95 V ($Mn^{4+} \rightarrow Mn^{3+}$) < 1.42 V ($Co^{4+} \rightarrow Co^{3+}$), indicating higher ease of reduction as the atomic number increases along the 3d period, which coincides with the decreasing $E_F[Va_O]$ trend, namely, 6.48−6.52 eV ($CaTiO_3$, $Ti^{4+} \rightarrow Ti^{3+}$) > 4.19−4.27 eV ($CaVO_3$, $V^{4+} \rightarrow V^{3+}$) > 2.25−2.27 eV ($CaMnO_3$, $Mn^{4+} \rightarrow Mn^{3+}$) > −1.37 eV ($CaCoO_3$, $Co^{4+} \rightarrow Co^{3+}$). Physically, introducing an oxygen vacancy reduces the material with two electrons. As a result, the ease of reducing the redox-active species becomes the predominant factor in determining $E_F[Va_O]$, consistent with our results.

Standard reduction potentials are not available for $Cr^{4+} \rightarrow Cr^{3+}$, $Fe^{4+} \rightarrow Fe^{3+}$, and $Ni^{4+} \rightarrow Ni^{3+}$. However, our predicted $E_F[Va_O]$ trends agree with predicted average intercalation voltages in layered $LiMO_2$ oxides,[76] where higher standard reduction potentials for the $M^{4+} \rightarrow M^{3+}$ results in higher average intercalation voltages. The anomalous increase in $E_F[Va_O]$ observed for $CaNiO_3$ is likely due to the occupation of antibonding e_g Ni states as Ni gets reduced from Ni^{4+} to Ni^{3+}. This is similar to the anomalous decrease in average intercalation voltage observed in $LiNiO_2$ when compared to other $LiMO_2$ oxides.[76] Indeed, $CaNiO_3$ exhibits a large band gap (∼1.43 eV, Table 1), with the conduction (valence) band edge states predominantly Ni 3d (O 2p, Figure S2a).

In the case of $CeMO_3$, there is a choice in redox activity between $Ce^{4+} \rightarrow Ce^{3+}$ and $M^{3+} \rightarrow M^{2+}$, depending on which oxidation states Ce and M atoms adopt in the bulk (Table 1). While Ce exhibits a +3 oxidation state in $CeScO_3$, $CeVO_3$, and $CeCrO_3$, it exhibits a +4 oxidation in $CeCoO_3$ and $CeNiO_3$. The oxidation state adopted by Ce depends on the relative standard reduction potential of $Ce^{4+} \rightarrow Ce^{3+}$ (1.61 V vs SHE) versus $M^{3+} \rightarrow M^{2+}$. In other words, the existence of Ce^{3+} in bulk $CeMO_3$ depends on the ease of reduction of Ce^{4+} versus M^{3+}. For example, the standard reduction potentials for Cr^{3+}

→ Cr^{2+} (−0.42 V vs SHE) and V^{3+} → V^{2+} (−0.26 V) are significantly more negative than Ce^{4+} → Ce^{3+} redox, while Co^{3+} → Co^{2+} is more positive (1.82 V). Thus, because Co^{3+} is easier to reduce than Ce^{4+}, it adopts the Co^{2+} oxidation state, whereas Ce exhibits the +3 state when coexisting with V or Cr. In the case of Ni, the Ni^{4+} → Ni^{2+} reduction potential (1.59 V) is quite similar to Ce^{4+} → Ce^{3+}, suggesting that Ce^{4+} and Ni^{2+} can coexist in $CeNiO_3$. With respect to $CeScO_3$, Ce is forced to adopt the +3 oxidation state since the highest stable oxidation state of Sc is +3. In addition, the conduction band edge in $CeScO_3$ is predominantly composed of Ce 4f states (Figure S2b), suggesting a Ce^{3+} → Ce^{2+} reduction upon Va_O formation. Thus, the transition metal redox (M^{3+} → M^{2+}) is largely responsible for determining $E_F[Va_O]$ in $CeVO_3$ and $CeCrO_3$, while the Ce^{4+} → Ce^{3+} sets $E_F[Va_O]$ in $CeCoO_3$ and $CeNiO_3$, with structural, stability, and electronic features also contributing to $E_F[Va_O]$. For example, although Ce is the redox-active species in both $CeCoO_3$ and $CeNiO_3$, the higher $E_F[Va_O]$ in $CeNiO_3$ correlates with the larger band gap in $CeNiO_3$ (0.22 eV, Table 1) versus $CeCoO_3$ (0.15 eV), since a higher band gap signifies a higher energy requirement for placing electrons in the conduction band.[77] On the other hand, the higher $E_F[Va_O]$ in metallic $CeVO_3$ versus metallic $CeCrO_3$ correlates better with thermodynamic stability trends (see section 5.1.3).

Under scenarios where both $CaMO_3$ and $CeMO_3$ exist, namely, V and Cr perovskites, the $CeMO_3$ perovskites exhibit a higher $E_F[Va_O]$ than the corresponding $CaMO_3$ structures (Figure 5). $E_F[Va_O]$s in $CeVO_3$ and $CeCrO_3$ are 4.19−4.27 and 5.22 eV, respectively, much higher than in $CaVO_3$ (2.67−2.77 eV) and $CaCrO_3$ (2.25−2.40 eV). The trend of higher $E_F[Va_O]$ in $CeMO_3$ vs $CaMO_3$ correlates with the standard reduction potentials of the redox-active cations. For example, it is easier to reduce V^{4+} → V^{3+} (0.34 V vs SHE) compared to V^{3+} → V^{2+} (−0.26 V). Hence, $CaVO_3$ more readily reduces upon Va_O formation than $CeVO_3$. Thus, M^{3+} → M^{2+} (M^{4+} → M^{3+}) reductions should correlate with a higher (lower) $E_F[Va_O]$ in oxide perovskites.

5.1.3. Thermodynamic Stability. Figure 6 displays the thermodynamic stability, as quantified by energy above or below the convex hull (E^{Hull}, *vide infra*) for all ternary $CaMO_3$ (orange bars) and $CeMO_3$ (blue bars) perovskites considered here. The 0 K phase diagram of a given system (e.g., Ce−Sc−O), also referred to as the ground-state convex hull, is a convex envelope of the lowest (Gibbs) energy states of the system. Thus, the convex hull is composed of all thermodynamically stable states of the system (e.g., Ce_2O_3, CeO_2, Sc_2O_3, etc.). Note that the thermodynamic (in)stability plotted in Figure 6 is mainly relevant for the stability and synthesizability of the perovskites considered at or near 298 K. Since STCH cycles occur at high temperatures (873−1773 K), it remains to be seen if our stability predictions hold at such high temperatures.

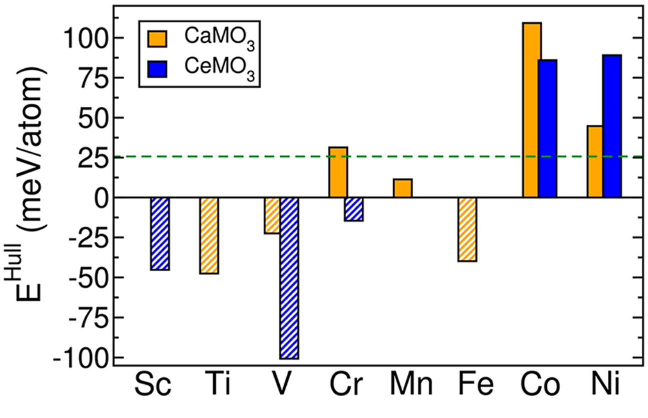

Figure 6. Energy above or below the ground-state convex hull (E^{Hull}) for all ternary perovskites considered in this work. Solid (hashed) bars indicate positive (negative) values of E^{hull}. A dashed green line signifies potential vibrational entropy stabilization of metastable structures at 298 K.

If a structure is metastable (or unstable), it has an $E^{Hull} > 0$ with the magnitude of E^{Hull} quantifying the energy release, or the extent of instability, upon decomposition to the stable states at that composition, where the stable states can be other binary or ternary compounds (see schematic in Figure S3a). For example, $CeNiO_3$ in Figure 6 has a positive E^{Hull} signifying its instability, with the absolute value of E^{Hull} (∼89 meV/atom) indicating the energy release upon decomposition to the stable states CeO_2 + NiO. CeO_2 and NiO are the stable states that are "adjacent" to (or competing with) $CeNiO_3$ on the convex hull. Additionally, the energy gained by decomposing $CeNiO_3$ to its adjacent states (CeO_2 + NiO) represents the largest energy gain (or the highest thermodynamic driving force) among other possible decomposition reactions (e.g., to Ce + Ni + O_2 formation instead of CeO_2 + NiO). Note that a structure exhibiting $E^{Hull} > 0$ does not necessarily mean that the structure cannot exist in nature. Indeed, several examples exist of metastable structures at 0 K that either become stable at higher temperatures (via entropic stabilization) or exist as a kinetically trapped state.[78−83] The dashed green line in Figure 6 represents the extent of vibrational entropy (∼26 meV/atom) that could stabilize a metastable (at 0 K) structure at 298 K, i.e., a structure with $E^{Hull} > 0$ meV/atom at 0 K being stabilized by entropy at 298 K. This has been used as a rule-of-thumb criterion for the existence of metastable structures in nature.[80,81]

Conventionally, all stable states at 0 K exhibit $E^{Hull} = 0$. To quantify the extent of stability of a given stable phase, we define an energy below the hull,[84] which is equivalent to the energy release when the stable phase is formed from its adjacent phases on the convex hull (Figure S3b). For example, Ce_2O_3 and Sc_2O_3 are the adjacent phases to $CeScO_3$ on the Ce−Sc−O ternary convex hull, i.e., if $CeScO_3$ were unstable, the Ce−Sc−O system would form a mixture of Ce_2O_3 and Sc_2O_3 at the composition of $CeScO_3$. Therefore, formation of $CeScO_3$ competes with the formation of Ce_2O_3 and Sc_2O_3. Thus, the E^{Hull} ∼ −45 meV/atom for $CeScO_3$ indicates the energy release if $CeScO_3$ is formed from Ce_2O_3 and Sc_2O_3. This E^{Hull} is also the smallest gain in energy (or the lowest thermodynamic driving force) to form $CeScO_3$ among possible formation reactions within the Ce−Sc−O ternary system (e.g., $CeScO_3$ formation from Ce + Sc + O_2 instead of Ce_2O_3 + Sc_2O_3 would release more energy). Table S1 of the SI tabulates the adjacent phases of all stable and unstable ternary and quaternary perovskites considered in this work.

Importantly, most ternary perovskite structures obtained from the ICSD are either thermodynamically stable ($E^{Hull} < 0$) or are marginally metastable (E^{Hull} ∼ 11 meV/atom for $CaMnO_3$, see Figure 6) at 0 K. Notably, $CaCrO_3$ exhibits a high degree of instability (E^{Hull} ∼ 31 meV/atom), with adjacent phases on the Ca−Cr−O phase diagram being CaO + $CaCrO_4$ + $CaCr_2O_4$ (Table S1). Given that solid-state reactions are slow at temperatures below 298 K, the decomposition of $CaCrO_3$ into three distinct solid phases could be prohibitively slow, allowing $CaCrO_3$ to exist as a kinetically trapped solid at low temperatures. Thus, as Figure 6 makes clear, $CaMO_3$ and $CeMO_3$ perovskites with an early-to-mid-row transition metal (i.e., M = Sc, Ti, V, Cr, Mn, and Fe) tend to be either stable or metastable. Early transition metals therefore should be viable additives to improve the thermodynamic stability of Ca- and/or Ce-based oxide perovskites.

Among the stable perovskites (hashed bars in Figure 6), $CeVO_3$ exhibits the highest degree of stability with $E^{\mathrm{Hull}} \sim -100$ meV/atom. Thus, the strong thermodynamic driving force to form $CeVO_3$ from its competing phases (Ce_2O_3 + V_2O_3, Table S1) highlights potentially facile synthesis. By contrast, all theoretical structures considered, namely, Co and Ni perovskites, are unstable, with $E^{\mathrm{Hull}} > 43$ meV/atom for all structures, which is well beyond the range of vibrational entropy stabilization (~26 meV/atom, dashed red line) at 298 K. Among the unstable structures, $CaCoO_3$ exhibits the highest $E^{\mathrm{Hull}} \sim 109$ meV/atom, with such a high degree of instability perhaps explaining the negative $E_F[Va_O]$ exhibited by the structure (Figure 5). Unfortunately, the high E^{Hull} (~86 meV/atom) for $CeCoO_3$ may preclude the technically viable use of $CeCoO_3$ within STCH cycles, despite its $E_F[Va_O]$ (3.67−3.72 eV, Figure 5) lying within the target window, due to potential difficulties in synthesis, high temperature stability, and eventual life of the material. Nevertheless, a recent study reported a successful synthesis of $CeCoO_3$ and $CeNiO_3$,[85] suggesting that $CeCoO_3$ may yet represent a feasible candidate for applications other than STCH.

5.2. Quaternary Ca−Ce−M−O Perovskites. *5.2.1. Oxygen Vacancy Formation Energy.* Figure 7 shows the oxygen vacancy formation energies in all the quaternary $Ca_{0.5}Ce_{0.5}MO_3$ perovskites considered here. Orange (blue) bars indicate perovskite structures obtained from ternary $CaMO_3$ ($CeMO_3$) structures. The hashed region on each bar is the variation caused by symmetrically distinct Va_O configurations in each quaternary structure, while the dashed red lines represent the target range for STCH (3.2−4.1 eV). Analogous to the trend observed in ternary $CaMO_3$ perovskites (Figure 5), both $CaMO_3$- and $CeMO_3$-based quaternary perovskites display a monotonically decreasing $E_F[Va_O]$ as M varies from Ti to Co. Both $CaMO_3$- and $CeMO_3$-based $Ca_{0.5}Ce_{0.5}NiO_3$ also exhibit an anomalously high $E_F[Va_O]$, similar to ternary $CaMO_3$ and $CeMO_3$ systems (Figure 5). The quaternary perovskites obtained from theoretical ternary structures (i.e., Co- and Ni-perovskites) exhibit higher variability in $E_F[Va_O]$ (extent of hashed regions, ~0.23−1.61 eV) compared to quaternaries derived from ICSD ternaries (~0.28−0.62 eV). $Ca_{0.5}Ce_{0.5}MnO_3$ and $Ca_{0.5}Ce_{0.5}FeO_3$ are the only candidate quaternaries that exhibit $E_F[Va_O]$ within the target range for STCH processes, namely, 3.65−3.96 and 3.77−4.06 eV, respectively. Additionally, both $Ca_{0.5}Ce_{0.5}MnO_3$ and $Ca_{0.5}Ce_{0.5}FeO_3$ exhibit $E_F[Va_O]$ lower than CeO_2 (~4−4.3 eV[42,52]), highlighting their potential viability for STCH. As discussed in section 5.3.3, we also expect $Ca_{0.5}Ce_{0.5}VO_3$ to be a potential candidate, as small energy differences between Ca−Ce configurations enable a large decrease in $E_F[Va_O]$ for an alternative Ca−Ce configuration, with the resulting $E_F[Va_O]$ near the target range for STCH. In the case of quinary $Ca_{0.5}Ce_{0.5}Ti_{0.5}Mg_{0.5}O_3$, we predict $E_F[Va_O]$ (3.83−4.36 eV) to be partially within the target range for STCH and comparable to $E_F[Va_O]$ in CeO_2.[42,52] Unfortunately, on-site magnetic moments suggest only a $Ce^{4+} \rightarrow Ce^{3+}$ reduction within $Ca_{0.5}Ce_{0.5}Ti_{0.5}Mg_{0.5}O_3$, thus excluding it as a potential candidate for simultaneous cation reduction.

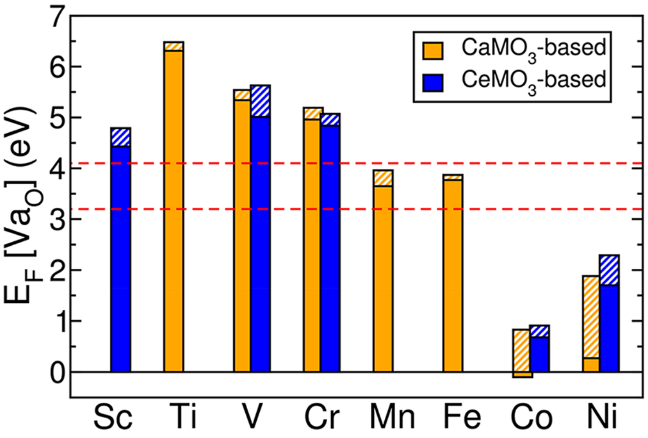

Figure 7. Oxygen vacancy formation energy of quaternary $Ca_{0.5}Ce_{0.5}MO_3$ perovskites derived from ternary $CaMO_3$ (orange bars) and $CeMO_3$ (blue bars) structures. The dashed red lines and hashed regions on each bar follow the notation used in Figure 5.

With the exception of $Ca_{0.5}Ce_{0.5}TiO_3$, $Ca_{0.5}Ce_{0.5}VO_3$, and $CaNiO_3$-based $Ca_{0.5}Ce_{0.5}NiO_3$, we find Ce to exhibit the +4 oxidation state in the bulk quaternary perovskites (Table 1), which is suitable for potential simultaneous redox activity. We find that Ce is the redox-active species in $Ca_{0.5}Ce_{0.5}ScO_3$ and $Ca_{0.5}Ce_{0.5}FeO_3$, whereas Co and Ni are redox-active in $Ca_{0.5}Ce_{0.5}CoO_3$ and $Ca_{0.5}Ce_{0.5}NiO_3$, respectively. The higher reduction potential of $Ce^{4+} \rightarrow Ce^{3+}$ (1.61 V vs SHE) explains the preferential reduction of Ce^{4+} in $Ca_{0.5}Ce_{0.5}FeO_3$ ($Fe^{3+} \rightarrow Fe^{2+}$ is 0.77 V vs SHE), while the higher $Co^{3+} \rightarrow Co^{2+}$ reduction potential (1.82 V vs SHE) enables Co^{3+} reduction instead of Ce^{4+} in $Ca_{0.5}Ce_{0.5}CoO_3$. In the case of $Ca_{0.5}Ce_{0.5}MnO_3$, we predict both Ce and Mn to be redox-active, whereas there is marginal evidence of simultaneous redox activity in $Ca_{0.5}Ce_{0.5}FeO_3$ (see section 5.3.2). For quaternaries where Ce is in its +3 oxidation state, the transition-metal cation, namely, Ti^{4+} in $Ca_{0.5}Ce_{0.5}TiO_3$ and V^{4+} in $Ca_{0.5}Ce_{0.5}VO_3$, undergoes reduction upon Va_O formation.

In ternary perovskites, a more positive $M^{3+} \rightarrow M^{2+}$ standard reduction potential than $Ce^{4+} \rightarrow Ce^{3+}$ dictates the presence of Ce^{4+} on the A site and M^{2+} on the B site. On the other hand, the presence of Ca^{2+} on the A site provides quaternary structures a choice of whether Ce^{3+} or M^{3+} oxidizes to the +4 state. Conventionally, if the $M^{3+} \rightarrow M^{4+}$ standard oxidation potential is less negative (or more favorable) than $Ce^{3+} \rightarrow Ce^{4+}$, the M^{3+} would be expected to attain +4 oxidation and Ce to adopt the +3 state. Indeed, the Ce in $Ca_{0.5}Ce_{0.5}TiO_3$ and $Ca_{0.5}Ce_{0.5}VO_3$ is in the +3 oxidation state, where $Ce^{3+} \rightarrow Ce^{4+}$ (−1.61 V vs SHE) is less favorable than $Ti^{3+} \rightarrow Ti^{4+}$ (−0.19 V) and $V^{3+} \rightarrow V^{4+}$ (−0.34 V). However, in $Ca_{0.5}Ce_{0.5}MnO_3$ and $Ca_{0.5}Ce_{0.5}CoO_3$, Ce adopts the +4 oxidation state despite the $Ce^{3+} \rightarrow Ce^{4+}$ reaction being less favorable than $Mn^{3+} \rightarrow Mn^{4+}$ (−0.95 V vs SHE) and $Co^{3+} \rightarrow Co^{4+}$ (−1.42 V), respectively, with $Ca_{0.5}Ce_{0.5}FeO_3$ also exhibiting Ce in the +4 state. Thus, chemical bonding and structural factors, specifically the presence of both Ca and Ce on the A site and the configuration that the Ca and Ce atoms adopt, seem to play a more significant role in determining the oxidation state and (potential) redox activity of Ce in quaternary perovskites than in ternary CeMO$_3$.

Comparing $E_F[Va_O]$ in ternary (Figure 5) and quaternary (Figure 7) perovskites, the addition of Ca (Ce) to CeMO$_3$ (CaMO$_3$) perovskites decreases (increases) the magnitude of $E_F[Va_O]$. For example, Ca addition to CeScO$_3$, CeVO$_3$, CeCrO$_3$, CeCoO$_3$, and CeNiO$_3$ causes a reduction in $E_F[Va_O]$ of ~2.34, 1.34, 0.38, 2.99, and 2.56 eV, respectively, when comparing the lowest $E_F[Va_O]$ in each ternary and quaternary perovskite. On the other hand, Ce addition to CaVO$_3$, CaCrO$_3$, CaMnO$_3$, CaFeO$_3$, and CaCoO$_3$ causes an increase in $E_F[Va_O]$ of ~1.15, 2.71, 1.40, 2.91, and 1.28 eV, respectively. Reduction of $E_F[Va_O]$ upon addition of an alkaline-earth cation into a LnBO$_3$ framework (where Ln = Lanthanide) has been observed before.[19,20,27,86−89] For example, the reduction in $E_F[Va_O]$ due to Sr addition in LaFeO$_3$ has been attributed to higher ionic character in the Sr−O bonds compared to La−O bonds and a better delocalization of the electrons introduced by Va$_O$ over the oxygen sublattice.[86] Analogously, Ce addition into CaMO$_3$ structures should exhibit the opposite effect to Sr addition in LaFeO$_3$,[86] causing an increased covalency of the A−O bonds and a reduced electron delocalization over the oxygen sublattice, which largely explains the increase in $E_F[Va_O]$ in Ca$_{0.5}$Ce$_{0.5}$MO$_3$ structures compared to their ternary CaMO$_3$ counterparts. Note that in the case of Ca$_{0.5}$Ce$_{0.5}$MnO$_3$ and Ca$_{0.5}$Ce$_{0.5}$FeO$_3$, the replacement of the $M^{4+} \rightarrow M^{3+}$ redox-activity in CaMO$_3$ by $Ce^{4+} \rightarrow Ce^{3+}$ and/or $M^{3+} \rightarrow M^{2+}$ in the quaternary structure also contributes to the increase in $E_F[Va_O]$. Thus, Ca/Ce addition could provide a useful handle to decrease/increase the $E_F[Va_O]$ toward a target value in candidate perovskites for STCH applications. Quantifying such effects will be the focus of future work.

5.2.2. Thermodynamic Stability. Figure 8 displays the thermodynamic stability at 0 K, as quantified by E^{Hull}, for all Ca$_{0.5}$Ce$_{0.5}$MO$_3$ perovskites considered here, with orange and blue bars indicating quaternaries derived from CaMO$_3$ and CeMO$_3$, respectively. The notation of E^{Hull} is identical to that in Figure 6, where the dashed green line indicates the extent of potential vibrational entropy stabilization at 298 K. In contrast to ternary CaMO$_3$ and CeMO$_3$, quaternary Ca$_{0.5}$Ce$_{0.5}$MO$_3$ perovskites have an additional configurational degree of freedom, namely, the sites occupied by Ca and Ce atoms in the A sublattice, which can also contribute potential entropic stabilization, especially at higher temperatures. Hence, the dashed purple line indicates the configurational entropy at 1273 K (~15 meV/atom, assuming ideal solution behavior) that can contribute in addition to the vibrational entropy stabilization (~26 meV/atom) at 298 K. We chose the temperature of 1273 K for the configurational entropy contribution since it is within the operating range of STCH cycles,[4,14] while other possible entropy threshold values can also be used.

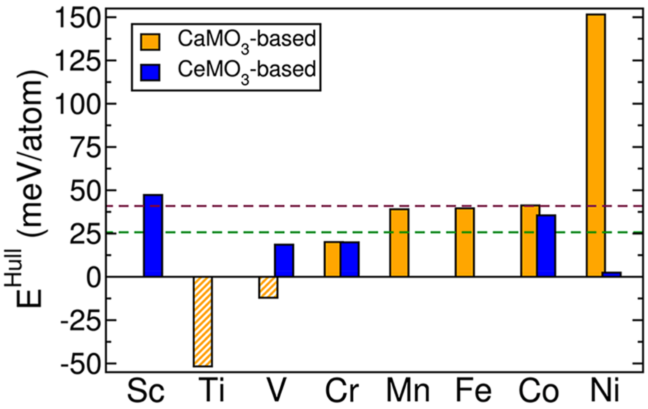

Figure 8. Energy above or below the hull for all quaternary Ca$_{0.5}$Ce$_{0.5}$MO$_3$ perovskites considered in this work. Dashed purple line indicates potential configurational entropy stabilization (at 1273 K), in addition to vibrational entropy stabilization (at 298 K, dashed green line). Orange and blue bars are CaMO$_3$- and CeMO$_3$-based quaternaries.

Among the quaternaries considered, we find only the Ca$_{0.5}$Ce$_{0.5}$TiO$_3$ and CaVO$_3$-based Ca$_{0.5}$Ce$_{0.5}$VO$_3$ to be thermodynamically stable at 0 K, exhibiting $E^{Hull} \sim -52$ and -12 meV/atom, respectively. Ca$_{0.5}$Ce$_{0.5}$CrO$_3$, Ca$_{0.5}$Ce$_{0.5}$MnO$_3$, Ca$_{0.5}$Ce$_{0.5}$FeO$_3$, and Ca$_{0.5}$Ce$_{0.5}$CoO$_3$ exhibit instability within the range of vibrational + configurational stabilization, i.e., $E^{Hull} < 41$ meV/atom, whereas Ca$_{0.5}$Ce$_{0.5}$ScO$_3$ and CaNiO$_3$-based Ca$_{0.5}$Ce$_{0.5}$NiO$_3$ have large E^{Hull} (>41 meV/atom), which does not bode well for their synthesis or potential use for STCH. Since Ca$_{1-x}$Ce$_x$MnO$_3$ perovskites ($0 \le x \le 0.2$) have been synthesized,[59,60,90] the Ca$_{0.5}$Ce$_{0.5}$MO$_3$ (M = Cr, Mn, Fe, and Co) structures may be synthesizable. Importantly, the level of instability among quaternary perovskites is higher than the corresponding ternaries, as quantified by the number of structures that are thermodynamically stable and possess higher E^{Hull} values. For example, there are six ternary perovskites (CeScO$_3$, CaTiO$_3$, CaVO$_3$, CeVO$_3$, CeCrO$_3$, and CaFeO$_3$, see Figure 6) that we predict to be thermodynamically stable at 0 K, while only two quaternary perovskites display $E^{Hull} < 0$ (hashed bars in Figure 8). Additionally, Ca$_{0.5}$Ce$_{0.5}$MnO$_3$ and Ca$_{0.5}$Ce$_{0.5}$NiO$_3$ structures exhibit higher E^{Hull} values, namely, 39 and 152 meV/atom, respectively, than the corresponding ternary CaMnO$_3$ (11 meV/atom) and CaNiO$_3$ (45 meV/atom) perovskites. In general, higher component systems tend to be entropy stabilized (particularly at higher temperatures), since the formation enthalpy "gain" in moving from $N - 1$ to N components is ~0 for $N > 3$.[91] In other words, it is easier to find structures that are stabilized by enthalpic contributions (and hence have $E^{Hull} \le 0$) for lower component systems ($N \le 3$), while it is easier to find entropy-stabilized structures for $N > 3$.[91] However, notable exceptions to the trend of increased instability in quaternaries include Ca$_{0.5}$Ce$_{0.5}$CrO$_3$ (20 meV/atom), and Ca$_{0.5}$Ce$_{0.5}$NiO$_3$ (2 meV/atom), which exhibit a reduced E^{Hull} compared to their corresponding ternary CaCrO$_3$ (31 meV/atom), and CeNiO$_3$ (89 meV/atom), respectively. Thus, Ce (Ca) addition to CaCrO$_3$ (CeNiO$_3$) can lead to stabilization of the bulk perovskite structure.

5.3. Candidate Ca−Ce−M−O Perovskites.

5.3.1. Ca$_{0.5}$Ce$_{0.5}$MnO$_3$. Panels a and b in Figure 9 display the projected density of states (pDOS) for pristine and defective Ca$_{0.5}$Ce$_{0.5}$MnO$_3$, respectively, with orange, green, red, violet, and brown lines indicating O 2p, Mn 3d, Ce 4f, Ce 5d, and Ca 4s states, respectively. Figure 9b shows an inset of the pDOS of defective Ca$_{0.5}$Ce$_{0.5}$MnO$_3$, focusing on the region around the Fermi level, with the full plot included as part of Figure S4a. Although SCAN+U calculations predict bulk Ca$_{0.5}$Ce$_{0.5}$MnO$_3$ to be metallic, the number of electron states near the Fermi level is quite low (~0.001 eV^{-1}). Given that SCAN+U calculations are known to underestimate band gaps in Mn oxides,[64] bulk Ca$_{0.5}$Ce$_{0.5}$MnO$_3$ is more likely to be a small-gap semiconductor. Qualitatively, the main difference between the

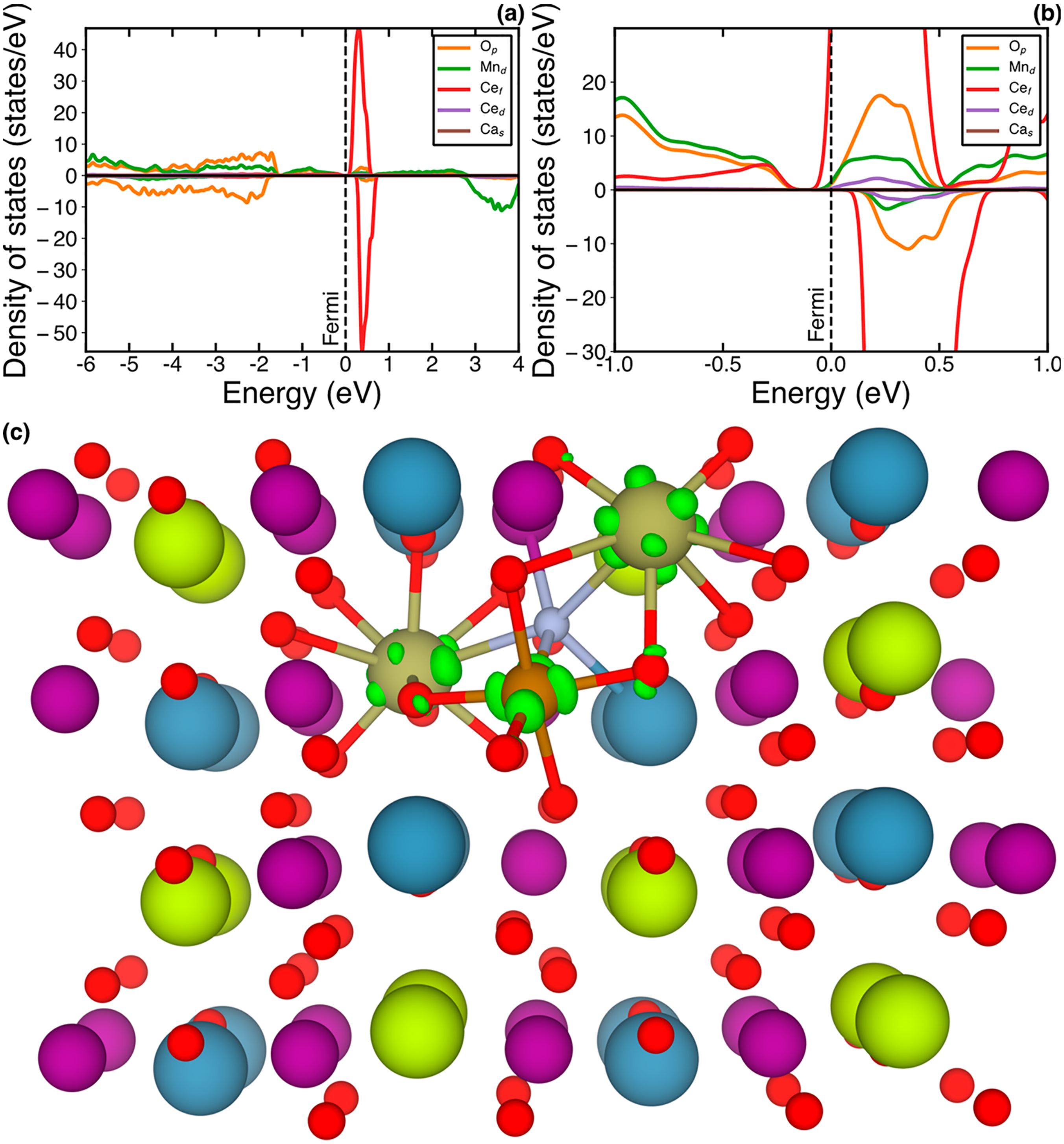

Figure 9. Projected DOS (pDOS) of pristine (panel a) and defective (panel b) $Ca_{0.5}Ce_{0.5}MnO_3$, with the zero on the energy scale set to the Fermi level (dashed black lines) in each panel. Positive (negative) pDOS indicates majority (minority) spin states. Panel c displays the electron density difference between the bulk and defective $Ca_{0.5}Ce_{0.5}MnO_3$, with the green isosurfaces (set to 0.009 e/bohr^3) representing regions of electron accumulation. Ca^{2+}, Ce^{4+}, Mn^{3+}, and O^{2-} ions are indicated by blue, yellow-green, purple, and red spheres, respectively. The gray sphere signifies the Va_O that is coordinated to one reduced Mn (brown), one other Mn (purple), two reduced Ce (olive green), and one Ca (blue).

pristine and defective $Ca_{0.5}Ce_{0.5}MnO_3$ pDOS (Figure 9 and Figure S4a) is the shift in the Fermi level, upon reduction, toward the unoccupied Ce 4f states, which form a peak close to the Fermi level (red lines in Figure 9a and b). Thus, these pDOS indicate that Ce^{4+} ions in $Ca_{0.5}Ce_{0.5}MnO_3$ undergo reduction with the introduction of a Va_O. However, a non-negligible number of Mn 3d (and O 2p) states that were unoccupied in the pristine structure acquire occupancy within the defective $Ca_{0.5}Ce_{0.5}MnO_3$, as highlighted by the presence of green and orange lines marginally below the Fermi level in Figure 9b. We also observe a change in the on-site magnetic moment of a Mn atom that neighbors the Va_O formed, toward Mn^{2+} (~4.4 μ_B), whereas the on-site moments of other Mn atoms indicate a +3 oxidation state (~3.8 μ_B), suggesting that a

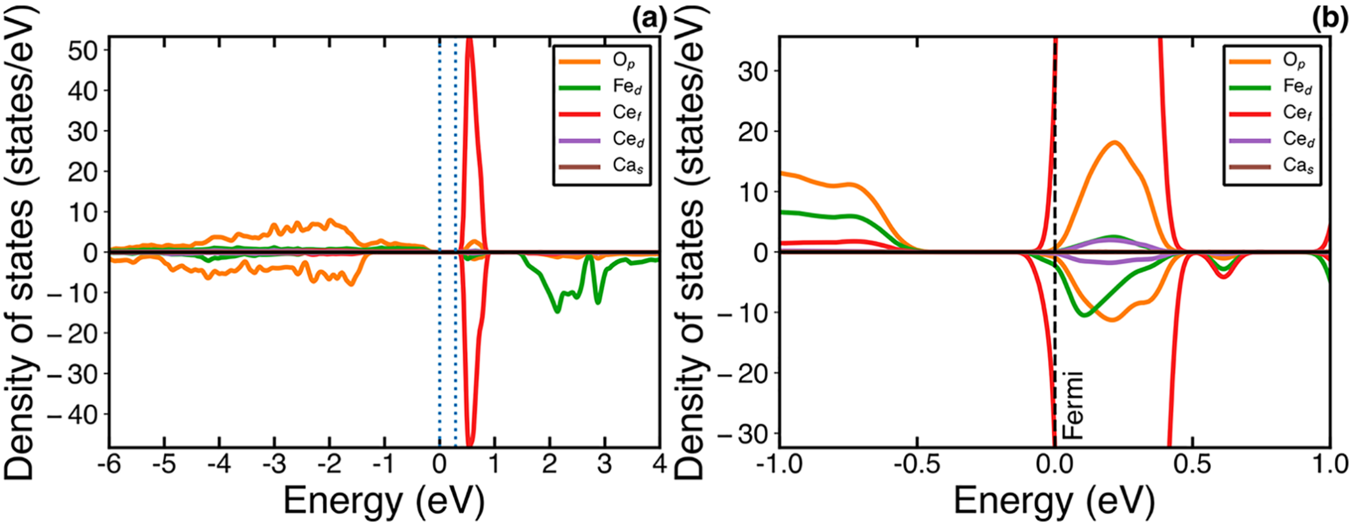

Figure 10. pDOS for (panel a) bulk and (panel b) defective $Ca_{0.5}Ce_{0.5}FeO_3$. Dashed blue lines in panel a indicate the valence and conduction band edges. Notations used in the figure are similar to those used in Figure 9.

Mn^{3+} reduces in addition to Ce^{4+}, resulting in simultaneous reduction across both the A and B sublattices. This simultaneous reduction is what we are seeking to find and the evidence is encouraging.

To verify further that both Ce^{4+} and Mn^{3+} reduce in $Ca_{0.5}Ce_{0.5}MnO_3$, we show the electron density difference between the pristine bulk and defective $Ca_{0.5}Ce_{0.5}MnO_3$ in Figure 9c. Green isosurfaces highlight regions of electron accumulation (upon Va_O formation), which are set to 0.009 e/bohr^3. Va_O formation reduces two Ce^{4+} ions (olive-green spheres) and one Mn^{3+} ion (brown sphere) adjacent to the Va_O. In particular, the isosurface around the brown Mn atom resembles a $d_{x^2-y^2}$ orbital, a strong indication that the generated electron localizes on one Mn, reducing it to a Mn^{2+} ion. In the case of Ce, the electron delocalizes over two neighboring Ce ions, partially reducing both ions, similar to behavior observed in oxygen-deficient CeO_2.[43,52,92] The electron delocalization over the Ce sites is also highlighted by the larger number of Ce 4f states below the Fermi level, compared to Mn 3d or O 2p states, in the pDOS of the defective perovskite (Figure 9b). A minor amount of electron accumulation appears on a few of the oxygen atoms that coordinate with the reduced Mn and Ce atoms, in agreement with the small number of O 2p states that exist in the defective pDOS below the Fermi level (Figure 9b). Therefore, based on the calculated pDOS, on-site magnetic moments, and electron density difference plots, we conclude that $Ca_{0.5}Ce_{0.5}MnO_3$ exhibits simultaneous reduction on both the Ce and Mn sublattices and therefore is a promising candidate for STCH and STCC.

Cation disorder on the A site—likely to be present at high temperatures—could affect our conclusions. We therefore also considered Va_O formation in a bulk $Ca_{0.5}Ce_{0.5}MnO_3$, where the Ca−Ce configuration exhibits a higher energy (~60 meV/atom) compared to the ground state and found $E_F[Va_O]$ to be 3.05−3.36 eV (Figure S5a), with the range in $E_F[Va_O]$ being due to symmetrically distinct Va_O configurations. As configurational disorder occurs on the Ca−Ce site, the energy of the bulk structure is expected to increase with respect to the ground state, coinciding with a drop in $E_F[Va_O]$ due to the breaking of "weaker" bonds in a high-energy bulk structure. However, the extent of the drop in $E_F[Va_O]$ with decreasing bulk stability is highly system-dependent. Hence, our calculation of $E_F[Va_O]$ in a higher energy configuration can be considered to be a proxy for Va_O formation in $Ca_{0.5}Ce_{0.5}MnO_3$ with disorder in the Ca−Ce sites. Importantly, the estimated $E_F[Va_O]$ in a higher energy bulk structure overlaps with our target range for STCH (3.2−4.1 eV), highlighting the viability of $Ca_{0.5}Ce_{0.5}MnO_3$.

5.3.2. $Ca_{0.5}Ce_{0.5}FeO_3$. Figure 10 displays the pDOS of bulk (panel a) and defective (panel b) $Ca_{0.5}Ce_{0.5}FeO_3$. Similar to Figure 9b, Figure 10b shows an inset of the pDOS with a focus around the Fermi level (dashed black line), with the full pDOS included in Figure S4b. Dotted blue lines in Figure 10a are the band edges within bulk $Ca_{0.5}Ce_{0.5}FeO_3$, which exhibits a gap of 0.29 eV. While the zero on the energy scale is set to the Fermi level in Figure 10b, it is set to the valence band edge in Figure 10a. Colored lines in both panels of Figure 10 have a notation similar to that of Figure 9 with the difference being that the green lines indicate Fe 3d states instead of Mn 3d.

Importantly, $Ca_{0.5}Ce_{0.5}FeO_3$ exhibits a semiconductor-to-metal transition upon Va_O formation, similar to behavior observed in defective CeO_2 and TiO_2.[93−95] The Fermi level moves from within the band gap in the nondefective structure toward the unoccupied Ce 4f states (red peaks in Figure 10) once the electrons from the Va_O are introduced. The large number of Ce 4f states at or below the Fermi level within defective $Ca_{0.5}Ce_{0.5}FeO_3$ (Figure 10b) is an indication of Ce^{4+} undergoing reduction within the structure. We also observe a small number of Fe 3d (green) and O 2p (orange) at or slightly below the Fermi level in Figure 10b, analogous to Figure 9b, possibly suggesting a simultaneous reduction of Fe^{3+} along with Ce^{4+}. However, we do not observe any changes in the on-site magnetic moments of Fe atoms that would indicate Fe^{2+} formation. Moreover, the electron density difference between bulk and defective $Ca_{0.5}Ce_{0.5}FeO_3$ (plotted in Figure S6) does not indicate electron accumulation on any of the Fe atoms that could suggest $Fe^{3+} \rightarrow Fe^{2+}$ reduction. Hence, there is marginal evidence, at best, for simultaneous Fe^{3+} and Ce^{4+} reduction in $Ca_{0.5}Ce_{0.5}FeO_3$. Nevertheless, the value of $E_F[Va_O]$ (3.77−4.06 eV) exhibited by $Ca_{0.5}Ce_{0.5}FeO_3$ is within the target region, which makes it a potentially interesting candidate for STCH and STCC. Further, the $E_F[Va_O]$ range

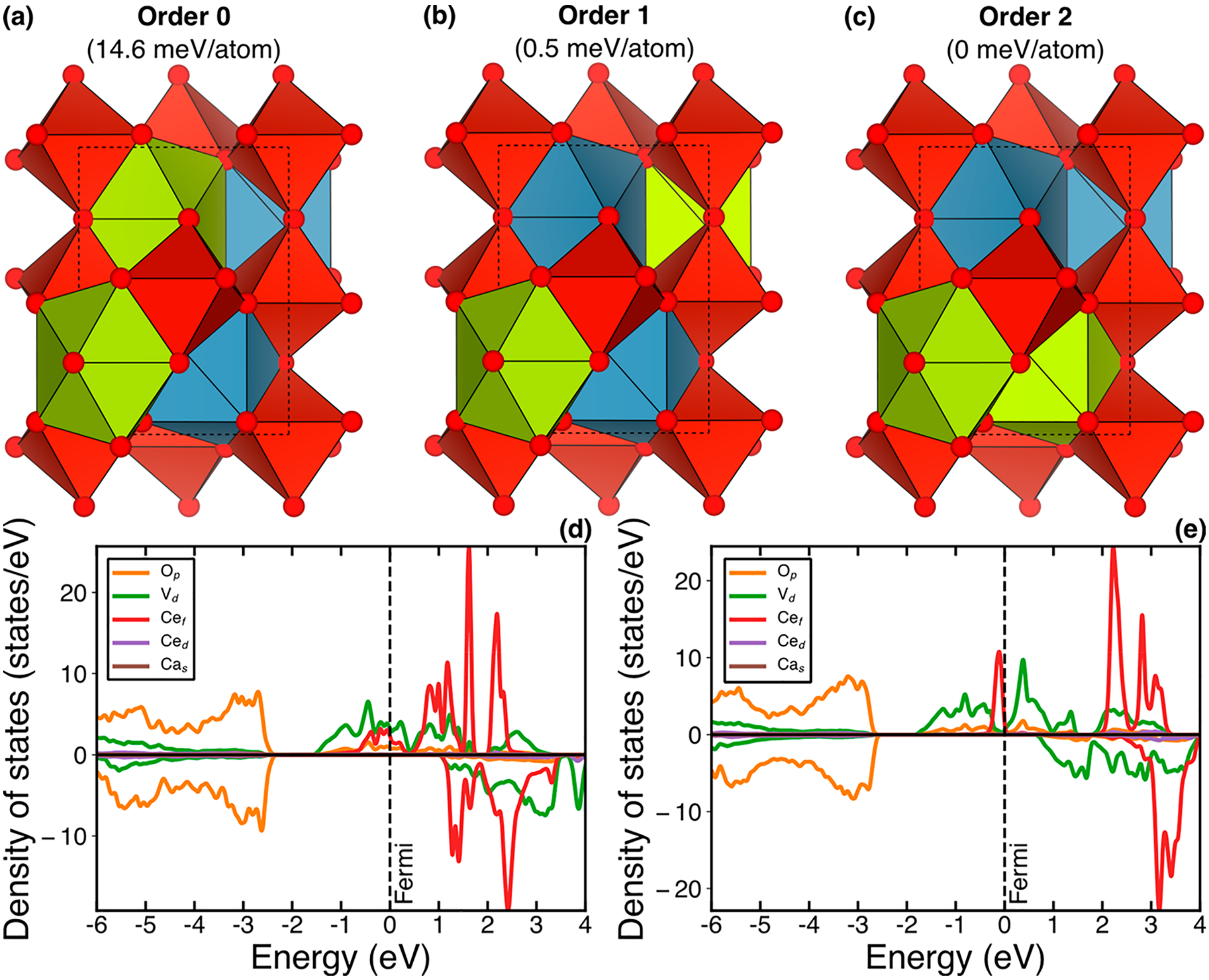

Figure 11. (a−c) Symmetrically distinct Ca−Ce configurations of $CeVO_3$-based $Ca_{0.5}Ce_{0.5}VO_3$, denoted Order 0, Order 1, and Order 2 and corresponding energies with respect to the ground-state configuration (Order 2). Blue, green, and red polyhedra signify Ca, Ce, and V atoms, respectively, while red spheres correspond to O atoms. The dashed black lines within the structures indicate the unit cell. (d,e) pDOS of nondefective Order 0 (d) and Order 2 (e) configurations, with the zero of the energy scale set to the Fermi level. Notations used in panels d and e are similar to those used in Figure 9.

changes only marginally (3.55−4.11 eV) when a higher energy Ca−Ce configuration within the bulk $Ca_{0.5}Ce_{0.5}FeO_3$ is considered (Figure S5b), indicating the relative insensitivity of $E_F[Va_O]$ with cation disorder in this system.

5.3.3. $CeVO_3$-based $Ca_{0.5}Ce_{0.5}VO_3$. Beyond $Ca_{0.5}Ce_{0.5}MnO_3$ and $Ca_{0.5}Ce_{0.5}FeO_3$, we also found $Ca_{0.5}Ce_{0.5}VO_3$ to be a potential candidate, depending on the Ca−Ce configuration that the system adopts within the A site. Figure 11a−c displays the three symmetrically distinct Ca−Ce configurations, denoted Order 0, Order 1, and Order 2, within the unit cell of the $CeVO_3$-based $Ca_{0.5}Ce_{0.5}VO_3$. The text annotation below each configuration name indicates the energy of that configuration with respect to the ground state. Thus, Order 2 is the ground state configuration while Order 0 and Order 1 have higher energies of 14.6 and 0.5 meV/atom, respectively, with respect to Order 2. Note that Order 2 has a E^{Hull} of 18.6 meV/atom (Figure 8), with the adjacent phases on the convex hull being $CaVO_3$ + $CeVO_3$ (Table S1). As a result, Order 0 and Order 1 exhibit an E^{Hull} of 33.2 and 19.1 meV/atom, respectively, well below the threshold E^{Hull} (~41 meV/atom) where configurational + vibrational entropy stabilization can occur (Figure 8). Thus, all configurations of $Ca_{0.5}Ce_{0.5}VO_3$ displayed in Figure 11 may be experimentally accessible.

Figures 11d and e display the pDOS of bulk Order 0 and Order 2 configurations, respectively, of $Ca_{0.5}Ce_{0.5}VO_3$. Orange, green, red, purple, and brown lines indicate O 2p, V 3d, Ce 4f, Ce 5d, and Ca 4s states, similar to Figures 9 and 10. Although both configurations are metallic, there are qualitative differences. For example, the distribution of unoccupied Ce 4f states (red peaks in Figure 11d) in Order 0 is pushed to higher energies in Order 2 (Figure 11e). Additionally, Order 2 exhibits a higher number of both unoccupied V 3d states (green peaks) and occupied Ce 4f states near the Fermi level than Order 0. As a result, upon Va_O formation, the electrons in Order 2 will occupy the V 3d states above the Fermi level, highlighting a $V^{4+} \rightarrow V^{3+}$ reduction. On the other hand, the electrons due to the Va_O in Order 0 can get delocalized over both Ce 4f and V 3d states that are present above the Fermi level, suggesting the reduction of both ions, and a consequent change in the $E_F[Va_O]$ compared to Order 2. Indeed, $E_F[Va_O]$ in Order 0 exhibits a range of 3.05−3.10 eV (slightly below the target window), which is significantly lower than Order 2 (5.34−5.54 eV, Figure 7), indicating that the contribution of both Ce and V to the reduction process can decrease the $E_F[Va_O]$. Thus, variations in the Ca−Ce configurations within $Ca_{0.5}Ce_{0.5}MO_3$ perovskites can cause significant changes in $E_F[Va_O]$, and subsequent studies are required to quantify this effect better. Importantly, given that Order 0 exhibits E^{Hull} within the 41 meV/atom threshold (Figures 11a and 8), if Order 0 can be accessed experimentally, it could be a promising candidate for STCH. Note that the synthesis and performance of V- (and Cr-)based perovskites may be affected by the volatility and high vapor pressure of the corresponding oxide and hydroxide compounds.[96,97]

6. DISCUSSION

We explored the Ca−Ce−M−O perovskite chemical space for potential candidates that exhibit both simultaneous redox activity and have $E_F[Va_O]$ within a specified target window suitable for STCH or STCC. Motivated by the potential impact of simultaneous cation redox (section 2), we developed a workflow to generate theoretical structures and evaluate $E_F[Va_O]$ in a systematic manner (section 4) across ternary $CaMO_3$, ternary $CeMO_3$, and quaternary $Ca_{0.5}Ce_{0.5}MO_3$ systems using SCAN+U calculations (section 3). Among ternary perovskites, only $CeCoO_3$ exhibited $E_F[Va_O]$ within the target range for STCH (Figure 5). However, the high thermodynamic instability of $CeCoO_3$ (Figure 6) reduces the likelihood of its practical use. In the case of higher-component perovskites, we found quaternary $Ca_{0.5}Ce_{0.5}MnO_3$ and $Ca_{0.5}Ce_{0.5}FeO_3$ to be promising candidates based on $E_F[Va_O]$ (Figure 7). The quinary $Ca_{0.5}Ce_{0.5}Ti_{0.5}Mg_{0.5}O_3$ also exhibits an $E_F[Va_O]$ that overlaps with the target window. We presented substantial evidence for simultaneous reduction of both Ce^{4+} and Mn^{3+} in $Ca_{0.5}Ce_{0.5}MnO_3$, thus making it a prime candidate to exhibit high ΔS_{red} (section 5.3.1). By contrast, $Ca_{0.5}Ce_{0.5}FeO_3$ does not exhibit simultaneous reduction and therefore is less attractive as a target for STCH. The difference between the Mn and Fe quaternary cases here are readily understood in terms of exchange driving forces (Mn^{3+} reducing to Mn^{2+} maximizes exchange stabilization in the half-filled d-shell of the latter) or lack thereof (reducing Fe^{3+} with its half-filled shell gains no exchange stabilization only Coulomb repulsion upon reduction to Fe^{2+}).[19] Although both $Ca_{0.5}Ce_{0.5}MnO_3$ and $Ca_{0.5}Ce_{0.5}FeO_3$ are not thermodynamically stable at 0 K, their E^{Hull} is below the 41 meV/atom threshold (Figure 8), indicating that they could be experimentally accessible at higher temperatures due to entropic stabilization. Additionally, we also found a higher energy Ca−Ce configuration in $CeVO_3$-based $Ca_{0.5}Ce_{0.5}VO_3$, which exhibits $E_F[Va_O]$ within the target window, which also could be a viable candidate if experimentally accessible (section 5.3.3).

In our analysis of the impact of simultaneous cation redox (section 2), we made two important assumptions: there is ideal solution configurational entropy on both reduced cation sublattices, and the electrons introduced due to Va_O distribute themselves equally across the A and B sites. These assumptions yield an upper bound on the oxygen off-stoichiometry obtained and hence the maximum influence of simultaneous cation redox on the oxygen evolution capacity. Indeed, maximizing the extent of (potential) configurational entropy arising from simultaneous cation redox was one of the major factors underpinning our considerations of the $Ca_{0.5}Ce_{0.5}MO_3$ compositions (section 2.1). However, the actual impact of simultaneous redox activity in a practical system will require further experimental investigation. Most materials typically exhibit ideal solution entropy only at high (∼melting point) temperatures. Moreover, the distribution of electrons over the reduced cations may not be equal, especially with the introduction of multiple oxygen vacancies. Instead, the distribution will depend upon the number of A or B states available in the DOS of the defective structure, where the DOS can change significantly as the Va_O concentration increases. Currently, there is little to no experimental information about this class of materials. Hence, it is possible that compositions involving proportions of Ca and Ce on the A site other than the 1:1 considered here could prove easier to synthesize, could exhibit lower kinetic limitations during TR and/or WS, and/or could have better cycle life in a STCH process. Thus, experimental investigations, especially of $Ca_{0.5}Ce_{0.5}MnO_3$, will determine (*i*) if a 1:1 proportion of Ca:Ce on the A site is experimentally viable (i.e., synthetically accessible); (*ii*) the actual gain in oxygen off-stoichiometry and configurational entropy is a result of simultaneous redox activity; and (*iii*) whether simultaneous cation redox exists and, if so, what the distribution of electrons is across the different redox-active cations.

While evaluating all the candidates considered in this work, we approximated $E_F[Va_O] \approx \Delta H_{red}$, consistent with previous studies.[30,31,98] However, it remains to be seen if this approximation is good enough for the quaternary perovskites considered here. For example, $CeO_{2-\delta}$ shows a highly nonlinear dependence of ΔH_{red} on δ, which has been well characterized both experimentally and theoretically.[42,44,52] The Va_O concentration in our supercells is ∼0.03 per ABO_3 formula unit, which is lower than what is ideally desired in a STCH cycle but is likely sufficient to compare the defect thermodynamics of a perovskite against CeO_2 (see Figure 1c) to identify candidate materials. Typically, quantifying the dependence of ΔH_{red} on the oxygen concentration requires more complex calculations, eventually resulting in building either a cluster expansion model[99] or a theoretical sublattice model.[52] Experimentally, careful calorimetry and/or thermal gravimetric analysis measurements provide information about the dependence of ΔH_{red} on the oxygen concentration. Such detailed follow-up theoretical/experimental studies will be useful to quantify off-stoichiometry at different temperatures and p_{O_2} and calibrate whether these material candidates can provide better performance attributes for STCH than ceria.

Apart from $E_F[Va_O] \approx \Delta H_{red}$, other major approximations in our calculations include the lack of inclusion of effects from vibrational entropy, lattice expansion (from 0 K to thermal reduction temperatures), and chemical expansion (due to oxygen off-stoichiometry) in the perovskite frameworks considered. Although these approximations may appear quite drastic, we point out that several previous theoretical studies have used similar approximations to our work and yet made highly useful theoretical predictions, often in agreement with experimental data.[17,28,40,52,77,100−102] Additionally, there are examples of studies that have screened for thermochemical water/CO_2 splitting candidates entirely using 0 K DFT-based calculations and identified promising candidates.[31,34,45] Hence, we believe that our approximations are justified, especially considering that the objective of this work is to identify perovskites that split water/CO_2 thermochemically while exhibiting simultaneous cation redox. As part of follow-up work, we intend to include these effects in studying the phase behavior of the proposed candidates (Mn-, Fe-, and V-based perovskites) under thermochemical conditions.

As noted in section 5.1.2, several factors, including structural, stability, electronic, electrostatic, and chemical bonding affect the absolute magnitude of $E_F[Va_O]$ in a given perovskite. For example, thermodynamically unstable structures typically exhibit lower $E_F[Va_O]$ than stable frameworks, as indicated by the lower $E_F[Va_O]$ in theoretical, ternary Co and Ni perovskites compared to ICSD structures (Figure 5). Moreover, at a given composition (e.g., $Ca_{0.5}Ce_{0.5}VO_3$), a higher energy configuration can yield a lower $E_F[Va_O]$ (see section 5.3.3). Similarly, structures with larger band gaps nominally exhibit higher $E_F[Va_O]$ than metallic structures, since there is a larger energy requirement to place electrons within the conduction band in nonmetallic structures than metallic phases. In the case of quaternary perovskites, the addition of Ca (Ce) to $CeMO_3$ ($CaMO_3$) structures tends to decrease (increase) the $E_F[Va_O]$ (Figure 7), which can be attributed to more ionic (covalent) bonding between Ca (Ce) and O and better (poorer) electron delocalization across the O sublattice.[86] In our work, we identified the standard reduction potential as a dominant criterion in dictating the monotonically decreasing $E_F[Va_O]$ trend in both $CaMO_3$ and $CeMO_3$ systems (Figure 5) and in determining the oxidation state of Ce in ternary $CeMO_3$ structures. However, notable exceptions to trends in standard reduction potentials arise while considering quaternary $Ca_{0.5}Ce_{0.5}MO_3$ systems (section 5.2.1). Hence, explaining local variations in $E_F[Va_O]$ may require model building that considers all factors that may contribute to $E_F[Va_O]$ and uses regression and/or advanced machine learning techniques to identify the dependence on each factor.[77] Previous attempts at building machine learning models have been restricted primarily to predicting bulk stabilities[56,103,104] and/or have been used to rationalize $E_F[Va_O]$ trends within a select system.[30,100] The computational workflow developed in this work (section 4) will be useful in generating data for developing better predictive models for $E_F[Va_O]$. Eventually, such advanced models may be able to predict, with quantitative accuracy, $E_F[Va_O]$ in other classes of perovskites and across compositions that may be difficult to model theoretically.

7. CONCLUSIONS

Researchers are actively considering oxide perovskites as candidate materials to improve the redox capacity of solar thermochemical water/CO_2 splitting materials, a promising technological pathway to produce renewable fuels and/or fuel precursors. However, most oxide perovskites only exhibit redox activity on the B site (within an ABO_3 framework), causing a decrease in the entropy of reduction per atom compared to the state-of-the-art CeO_2. Here, we explored the Ca−Ce−M−O chemical space (where M = Sc, Ti, V, Cr, Mn, Fe, Co, and Ni) to identify perovskite compounds that might exhibit simultaneous redox activity on both the A (Ca + Ce) and B (3d metal) sites to increase the entropy of reduction over single-cation redox. Specifically, we developed a computational workflow using SCAN+*U* calculations to systematically evaluate the oxygen vacancy formation energy, the thermodynamic stability at 0 K, and the electronic properties of pristine and defective structures in ternary $CaMO_3$, ternary $CeMO_3$, and quaternary $Ca_{0.5}Ce_{0.5}MO_3$ perovskites, as well as calculating $E_F[Va_O]$ in quinary $Ca_{0.5}Ce_{0.5}Ti_{0.5}Mg_{0.5}O_3$. On the basis of our calculations, we found ternary $CeCoO_3$, quaternary $Ca_{0.5}Ce_{0.5}MnO_3$, and quaternary $Ca_{0.5}Ce_{0.5}FeO_3$ to exhibit $E_F[Va_O]$ in our target range (3.2−4.1 eV) and quinary $Ca_{0.5}Ce_{0.5}Ti_{0.5}Mg_{0.5}O_3$ to display near-target $E_F[Va_O]$ for the STCH application. Importantly, we found $Ca_{0.5}Ce_{0.5}MnO_3$ to display simultaneous reduction of both Ce^{4+} and Mn^{3+} cations, based on calculated densities of states, on-site Mn magnetic moments, and electron density differences between pristine and defective structures. Accounting for thermodynamic stability at 0 K, we expect both $Ca_{0.5}Ce_{0.5}MnO_3$ and $Ca_{0.5}Ce_{0.5}FeO_3$ to be promising candidates apart from $Ca_{0.5}Ce_{0.5}VO_3$, which can achieve an $E_F[Va_O]$ within our target if its metastable configuration(s) can be stabilized and accessed. Additionally, we found the trends in standard reduction potentials of cations to be a predominant descriptor in explaining the monotonically decreasing $E_F[Va_O]$ as M is varied from Ti to Co in ternary $CaMO_3$ and $CeMO_3$ perovskites. However, other factors (structural, electronic, etc.) play a larger role in determining the absolute values and qualitative trends of $E_F[Va_O]$ in quaternary $Ca_{0.5}Ce_{0.5}MO_3$. We urge experimental evaluation and validation of the candidates that emerged from this work, particularly $Ca_{0.5}Ce_{0.5}MnO_3$, to examine the practical redox capacity gains in a STCH process and further theoretical studies to predict quantitatively the oxygen vacancy formation energies in perovskites and other oxides.

■ ASSOCIATED CONTENT

Supporting Information

The Supporting Information is available free of charge at https://pubs.acs.org/doi/10.1021/acs.chemmater.0c02912.

> Initial structures of the quaternary perovskite compositions considered; projected density of states of $CaNiO_3$, $CeScO_3$, $Ca_{0.5}Ce_{0.5}MnO_3$, and $Ca_{0.5}Ce_{0.5}FeO_3$; illustration of energy above and below hull; list of adjacent states at 0 K for all ternary and quaternary compounds considered in this work; high-energy Ca−Ce configurations in $Ca_{0.5}Ce_{0.5}MnO_3$ and $Ca_{0.5}Ce_{0.5}FeO_3$; electron density difference isosurface plot between pure and defective $Ca_{0.5}Ce_{0.5}FeO_3$ (PDF)

■ AUTHOR INFORMATION

Corresponding Author

Emily A. Carter − *Department of Mechanical and Aerospace Engineering, Princeton University, Princeton, New Jersey 08544-5263, United States; Office of the Chancellor and Department of Chemical and Biomolecular Engineering, University of California, Los Angeles, Los Angeles, California 90095-1405, United States;* orcid.org/0000-0001-7330-7554; Email: eac@princeton.edu

Authors

Gopalakrishnan Sai Gautam − *Department of Mechanical and Aerospace Engineering, Princeton University, Princeton, New Jersey 08544-5263, United States;* orcid.org/0000-0002-1303-0976

Ellen B. Stechel − *ASU Lightworks and the School of Molecular Sciences, Arizona State University, Tempe,* *Arizona 85287-5402, United States;* orcid.org/0000-0002-5379-2908

Complete contact information is available at:
https://pubs.acs.org/10.1021/acs.chemmater.0c02912

Notes

The authors declare no competing financial interest.

■ ACKNOWLEDGMENTS

E.A.C. and E.B.S. gratefully acknowledge research and funding support from the HydroGEN Advanced Water Splitting Materials Consortium, established as part of the Energy Materials Network under the U.S. Department of Energy, Office of Energy Efficiency and Renewable Energy, Fuel Cell Technologies Office, under Award No. DE-EE0008090. The authors thank Princeton Research Computing resources at Princeton University, a consortium of groups including the Princeton Institute for Computational Science and Engineering and the Princeton University Office of Information Technology's Research Computing department. The authors also acknowledge computational resources sponsored by the Department of Energy's Office of Energy Efficiency and Renewable Energy located at the National Renewable Energy Laboratory. The views and opinions of the authors expressed herein do not necessarily state or reflect those of the United States Government or any agency thereof. Neither the United States Government nor any agency thereof, nor any of their employees, makes any warranty, expressed or implied, or assumes any legal liability or responsibility for the accuracy, completeness, or usefulness of any information, apparatus, product, or process disclosed, or represents that its use would not infringe privately owned rights.

■ REFERENCES

(1) Steinfeld, A. Solar Thermochemical Production of Hydrogen—A Review. *Sol. Energy* **2005**, *78* (5), 603−615.

(2) Rao, C. N. R.; Dey, S. Solar Thermochemical Splitting of Water to Generate Hydrogen. *Proc. Natl. Acad. Sci. U. S. A.* **2017**, *114* (51), 13385−13393.

(3) Steinfeld, A.; Sanders, S.; Palumbo, R. Design Aspects of Solar Thermochemical Engineering—A Case Study: Two-Step Water-Splitting Cycle Using the Fe_3O_4/FeO Redox System. *Sol. Energy* **1999**, *65* (1), 43−53.

(4) Carrillo, R. J.; Scheffe, J. R. Advances and Trends in Redox Materials for Solar Thermochemical Fuel Production. *Sol. Energy* **2017**, *156*, 3−20.

(5) Siegel, N. P.; Miller, J. E.; Ermanoski, I.; Diver, R. B.; Stechel, E. B. Factors Affecting the Efficiency of Solar Driven Metal Oxide Thermochemical Cycles. *Ind. Eng. Chem. Res.* **2013**, *52* (9), 3276−3286.

(6) Kim, J.; Johnson, T. A.; Miller, J. E.; Stechel, E. B.; Maravelias, C. T. Fuel Production from CO_2 Using Solar-Thermal Energy: System Level Analysis. *Energy Environ. Sci.* **2012**, *5* (9), 8417.

(7) Rao, C. N. R.; Dey, S. Generation of H_2 and CO by Solar Thermochemical Splitting of H_2O and CO_2 by Employing Metal Oxides. *J. Solid State Chem.* **2016**, *242*, 107−115.

(8) Vickers, J. W.; Dinh, H. N.; Randolph, K.; Weber, A. Z.; McDaniel, A. H.; Boardman, R.; Ogitsu, T.; Colon-Mercado, H.; Peterson, D.; Miller, E. L. HydroGEN: An AWSM Energy Materials Network. *ECS Trans.* **2018**, *85* (11), 3−14.

(9) Miller, J. E.; McDaniel, A. H.; Allendorf, M. D. Considerations in the Design of Materials for Solar-Driven Fuel Production Using Metal-Oxide Thermochemical Cycles. *Adv. Energy Mater.* **2014**, *4* (2), 1300469.

(10) Budama, V. K.; Johnson, N. G.; McDaniel, A.; Ermanoski, I.; Stechel, E. B. Thermodynamic Development and Design of a Concentrating Solar Thermochemical Water-Splitting Process for Co-Production of Hydrogen and Electricity. *Int. J. Hydrogen Energy* **2018**, *43* (37), 17574−17587.

(11) Centi, G.; Perathoner, S. Towards Solar Fuels from Water and CO_2. *ChemSusChem* **2010**, *3* (2), 195−208.

(12) Battraw, M.; Albrecht, K.; McDaniel, A. H. *Standardizing Solar-to-Hydrogen Efficiency Calculations for the Evaluation of New Water Splitting Materials*; Sandia National Laboratories: Albuquerque, NM; Livermore, CA, 2018.

(13) Bulfin, B.; Vieten, J.; Agrafiotis, C.; Roeb, M.; Sattler, C. Applications and Limitations of Two Step Metal Oxide Thermochemical Redox Cycles; a Review. *J. Mater. Chem. A* **2017**, *5* (36), 18951−18966.

(14) Stechel, E. B.; Miller, J. E.; Ermanoski, I. Materials Thermodynamic Limits in Thermochemical Fuel Production. In preparation.

(15) Hao, Y.; Yang, C.-K.; Haile, S. M. Ceria−Zirconia Solid Solutions ($Ce_{1-x}Zr_xO_{2-\delta}$, $x \leq 0.2$) for Solar Thermochemical Water Splitting: A Thermodynamic Study. *Chem. Mater.* **2014**, *26* (20), 6073−6082.

(16) Chueh, W. C.; Haile, S. M. Ceria as a Thermochemical Reaction Medium for Selectively Generating Syngas or Methane from H_2O and CO_2. *ChemSusChem* **2009**, *2* (8), 735−739.

(17) Naghavi, S. S.; Emery, A. A.; Hansen, H. A.; Zhou, F.; Ozoliņš, V.; Wolverton, C. Giant Onsite Electronic Entropy Enhances the Performance of Ceria for Water Splitting. *Nat. Commun.* **2017**, *8*, 285.

(18) Pappacena, A.; Rancan, M.; Armelao, L.; Llorca, J.; Ge, W.; Ye, B.; Lucotti, A.; Trovarelli, A.; Boaro, M. New Insights into the Dynamics That Control the Activity of Ceria−Zirconia Solid Solutions in Thermochemical Water Splitting Cycles. *J. Phys. Chem. C* **2017**, *121* (33), 17746−17755.

(19) Pavone, M.; Ritzmann, A. M.; Carter, E. A. Quantum-Mechanics-Based Design Principles for Solid Oxide Fuel Cell Cathode Materials. *Energy Environ. Sci.* **2011**, *4* (12), 4933.

(20) Muñoz-García, A. B.; Ritzmann, A. M.; Pavone, M.; Keith, J. A.; Carter, E. A. Oxygen Transport in Perovskite-Type Solid Oxide Fuel Cell Materials: Insights from Quantum Mechanics. *Acc. Chem. Res.* **2014**, *47* (11), 3340−3348.

(21) O'Hayre, R.; Cha, S.-W.; Colella, W.; Prinz, F. B. *Fuel Cell Fundamentals*; John Wiley & Sons, Inc: Hoboken, NJ, 2016.

(22) Norby, T. Proton Conductivity in Perovskite Oxides. In *Perovskite Oxide for Solid Oxide Fuel Cells*; Ishihara, T., Ed.; Springer: Boston, MA, 2009; pp 217−241.

(23) Bowen, C. R.; Kim, H. A.; Weaver, P. M.; Dunn, S. Piezoelectric and Ferroelectric Materials and Structures for Energy Harvesting Applications. *Energy Environ. Sci.* **2014**, *7* (1), 25−44.

(24) Maignan, A.; Hébert, S.; Pi, L.; Pelloquin, D.; Martin, C.; Michel, C.; Hervieu, M.; Raveau, B. Perovskite Manganites and Layered Cobaltites: Potential Materials for Thermoelectric Applications. *Cryst. Eng.* **2002**, *5* (3−4), 365−382.

(25) Vieten, J.; Bulfin, B.; Call, F.; Lange, M.; Schmücker, M.; Francke, A.; Roeb, M.; Sattler, C. Perovskite Oxides for Application in Thermochemical Air Separation and Oxygen Storage. *J. Mater. Chem. A* **2016**, *4* (35), 13652−13659.

(26) Scheffe, J. R.; Weibel, D.; Steinfeld, A. Lanthanum−Strontium−Manganese Perovskites as Redox Materials for Solar Thermochemical Splitting of H_2O and CO_2. *Energy Fuels* **2013**, *27* (8), 4250−4257.

(27) McDaniel, A. H.; Miller, E. C.; Arifin, D.; Ambrosini, A.; Coker, E. N.; O'Hayre, R.; Chueh, W. C.; Tong, J. Sr- and Mn-Doped $LaAlO_{3-\delta}$ for Solar Thermochemical H_2 and CO Production. *Energy Environ. Sci.* **2013**, *6*, 2424−2428.

(28) Barcellos, D. R.; Sanders, M. D.; Tong, J.; McDaniel, A. H.; O'Hayre, R. P. $BaCe_{0.25}Mn_{0.75}O_{3-\delta}$—a Promising Perovskite-Type Oxide for Solar Thermochemical Hydrogen Production. *Energy Environ. Sci.* **2018**, *11*, 3256−3265.

(29) Yang, C.-K.; Yamazaki, Y.; Aydin, A.; Haile, S. M. Thermodynamic and Kinetic Assessments of Strontium-Doped Lanthanum Manganite Perovskites for Two-Step Thermochemical Water Splitting. *J. Mater. Chem. A* **2014**, *2* (33), 13612−13623.

(30) Deml, A. M.; Stevanović, V.; Holder, A. M.; Sanders, M.; O'Hayre, R.; Musgrave, C. B. Tunable Oxygen Vacancy Formation Energetics in the Complex Perovskite Oxide $Sr_xLa_{1-x}Mn_yAl_{1-y}O_3$. *Chem. Mater.* **2014**, *26*, 6595−6602.

(31) Emery, A. A.; Saal, J. E.; Kirklin, S.; Hegde, V. I.; Wolverton, C. High-Throughput Computational Screening of Perovskites for Thermochemical Water Splitting Applications. *Chem. Mater.* **2016**, *28* (16), 5621−5634.

(32) Barcellos, D. R.; Coury, F. G.; Emery, A.; Sanders, M.; Tong, J.; McDaniel, A.; Wolverton, C.; Kaufman, M.; O'Hayre, R. Phase Identification of the Layered Perovskite $Ce_xSr_{2-x}MnO_4$ and Application for Solar Thermochemical Water Splitting. *Inorg. Chem.* **2019**, *58* (12), 7705−7714.

(33) McDaniel, A. H.; Ambrosini, A.; Coker, E. N.; Miller, J. E.; Chueh, W. C.; O'Hayre, R.; Tong, J. Nonstoichiometric Perovskite Oxides for Solar Thermochemical H_2 and CO Production. *Energy Procedia* **2014**, *49*, 2009−2018.

(34) Emery, A. A.; Wolverton, C. High-Throughput DFT Calculations of Formation Energy, Stability and Oxygen Vacancy Formation Energy of ABO_3 Perovskites. *Sci. Data* **2017**, *4* (1), 170153.

(35) Nalbandian, L.; Evdou, A.; Zaspalis, V. $La_{1-x}Sr_xMO_3$ (M = Mn, Fe) Perovskites as Materials for Thermochemical Hydrogen Production in Conventional and Membrane Reactors. *Int. J. Hydrogen Energy* **2009**, *34* (17), 7162−7172.

(36) Jiang, Q.; Tong, J.; Zhou, G.; Jiang, Z.; Li, Z.; Li, C. Thermochemical CO_2 Splitting Reaction with Supported $La_xA_{1-x}Fe_yB_{1-y}O_3$ (A = Sr, Ce, B = Co, Mn; $0 \leqslant x, y \leqslant 1$) Perovskite Oxides. *Sol. Energy* **2014**, *103*, 425−437.

(37) Vieten, J.; Bulfin, B.; Huck, P.; Horton, M.; Guban, D.; Zhu, L.; Lu, Y.; Persson, K. A.; Roeb, M.; Sattler, C. Materials Design of Perovskite Solid Solutions for Thermochemical Applications. *Energy Environ. Sci.* **2019**, *12* (4), 1369−1384.

(38) Vieten, J. *Perovskite Materials Design for Two-Step Solar-Thermochemical Redox Cycles*; Technische Universität Dresden, 2019.

(39) McDaniel, A. H.; Stechel, E. B.; Johnson, N.; Siegel, N.; O'Hayre, R.; Sanders, M.; Wolverton, C.; Chueh, W. *High Efficiency Solar Thermochemical Reactor for Hydrogen Production*; Sandia National Laboratories: Albuquerque, NM; Livermore, CA, 2016.

(40) Meredig, B.; Wolverton, C. First-Principles Thermodynamic Framework for the Evaluation of Thermochemical H_2O- or CO_2-Splitting Materials. *Phys. Rev. B: Condens. Matter Mater. Phys.* **2009**, *80* (24), 245119.

(41) Lany, S. Communication: The Electronic Entropy of Charged Defect Formation and Its Impact on Thermochemical Redox Cycles. *J. Chem. Phys.* **2018**, *148* (7), 071101.

(42) Zinkevich, M.; Djurovic, D.; Aldinger, F. Thermodynamic Modelling of the Cerium−Oxygen System. *Solid State Ionics* **2006**, *177* (11−12), 989−1001.

(43) Skorodumova, N. V.; Simak, S. I.; Lundqvist, B. I.; Abrikosov, I. A.; Johansson, B. Quantum Origin of the Oxygen Storage Capability of Ceria. *Phys. Rev. Lett.* **2002**, *89* (16), 166601.

(44) Gopal, C. B.; van de Walle, A. Ab Initio Thermodynamics of Intrinsic Oxygen Vacancies in Ceria. *Phys. Rev. B: Condens. Matter Mater. Phys.* **2012**, *86*, 134117.

(45) Naghavi, S. S.; He, J.; Wolverton, C. $CeTi_2O_6$ —A Promising Oxide for Solar Thermochemical Hydrogen Production. *ACS Appl. Mater. Interfaces* **2020**, *12* (19), 21521−21527.

(46) Zhai, S.; Rojas, J.; Ahlborg, N.; Lim, K.; Toney, M. F.; Jin, H.; Chueh, W. C.; Majumdar, A. The Use of Poly-Cation Oxides to Lower the Temperature of Two-Step Thermochemical Water Splitting. *Energy Environ. Sci.* **2018**, *11* (8), 2172−2178.

(47) Hohenberg, P.; Kohn, W. Inhomogeneous Electron Gas. *Phys. Rev.* **1964**, *136* (3B), B864−B871.

(48) Kohn, W.; Sham, L. J. Self-Consistent Equations Including Exchange and Correlation Effects. *Phys. Rev.* **1965**, *140* (4A), A1133−A1138.

(49) Freysoldt, C.; Grabowski, B.; Hickel, T.; Neugebauer, J.; Kresse, G.; Janotti, A.; Van de Walle, C. G. First-Principles Calculations for Point Defects in Solids. *Rev. Mod. Phys.* **2014**, *86* (1), 253−305.

(50) Canepa, P.; Sai Gautam, G.; Broberg, D.; Bo, S.-H.; Ceder, G. Role of Point Defects in Spinel Mg Chalcogenide Conductors. *Chem. Mater.* **2017**, *29* (22), 9657−9667.

(51) Sai Gautam, G.; Senftle, T. P.; Carter, E. A. Understanding the Effects of Cd and Ag Doping in Cu_2ZnSnS_4 Solar Cells. *Chem. Mater.* **2018**, *30* (14), 4543−4555.

(52) Sai Gautam, G.; Stechel, E. B.; Carter, E. A. A First-Principles-Based Sub-Lattice Formalism for Predicting Off-Stoichiometry in Materials for Solar Thermochemical Applications: The Example of Ceria. *Adv. Theory Simulations* **2020**, *3*, 2000112.

(53) Wang, H.-F.; Gong, X.-Q.; Guo, Y.-L.; Guo, Y.; Lu, G. Z.; Hu, P. A Model to Understand the Oxygen Vacancy Formation in Zr-Doped CeO_2: Electrostatic Interaction and Structural Relaxation. *J. Phys. Chem. C* **2009**, *113* (23), 10229−10232.

(54) *NIST Chemistry WebBook, NIST Standard Reference Database Number 69*; Linstorm, P. J., Mallard, W. G., Eds.; National Institute of Standards and Technology: Gaithersburg, MD, 2019.

(55) Goldschmidt, V. M. Die Gesetze Der Krystallochemie. *Naturwissenschaften* **1926**, *14* (21), 477−485.

(56) Bartel, C. J.; Sutton, C.; Goldsmith, B. R.; Ouyang, R.; Musgrave, C. B.; Ghiringhelli, L. M.; Scheffler, M. New Tolerance Factor to Predict the Stability of Perovskite Oxides and Halides. *Sci. Adv.* **2019**, *5* (2), eaav0693.

(57) Long, O. Y.; Sai Gautam, G.; Carter, E. A. Evaluating Optimal U for 3d Transition-Metal Oxides within the SCAN+U Framework. *Phys. Rev. Mater.* **2020**, *4* (4), 045401.

(58) Shannon, R. D.; Prewitt, C. T. Effective Ionic Radii in Oxides and Fluorides. *Acta Crystallogr., Sect. B: Struct. Crystallogr. Cryst. Chem.* **1969**, *25*, 925−946.

(59) Zeng, Z.; Greenblatt, M.; Croft, M. Charge Ordering and Magnetoresistance of Ca1-XCexMnO3. *Phys. Rev. B: Condens. Matter Mater. Phys.* **2001**, *63* (22), 224410.

(60) Caspi, E. N.; Avdeev, M.; Short, S.; Jorgensen, J. D.; Lobanov, M. V.; Zeng, Z.; Greenblatt, M.; Thiyagarajan, P.; Botez, C. E.; Stephens, P. W. Structural and Magnetic Phase Diagram of the Two-Electron-Doped $(Ca_{1-x}Ce_x)MnO_3$ System: Effects of Competition among Charge, Orbital, and Spin Ordering. *Phys. Rev. B: Condens. Matter Mater. Phys.* **2004**, *69* (10), 104402.

(61) Kresse, G.; Hafner, J. Ab Initio Molecular Dynamics for Liquid Metals. *Phys. Rev. B: Condens. Matter Mater. Phys.* **1993**, *47* (1), 558−561.

(62) Kresse, G.; Furthmüller, J. Efficient Iterative Schemes for Ab Initio Total-Energy Calculations Using a Plane-Wave Basis Set. *Phys. Rev. B: Condens. Matter Mater. Phys.* **1996**, *54* (16), 11169−11186.

(63) Kresse, G.; Joubert, D. From Ultrasoft Pseudopotentials to the Projector Augmented-Wave Method. *Phys. Rev. B: Condens. Matter Mater. Phys.* **1999**, *59* (3), 1758−1775.

(64) Sai Gautam, G.; Carter, E. A. Evaluating Transition Metal Oxides within DFT-SCAN and SCAN+U Frameworks for Solar Thermochemical Applications. *Phys. Rev. Mater.* **2018**, *2* (9), 095401.

(65) Anisimov, V. I.; Zaanen, J.; Andersen, O. K. Band Theory and Mott Insulators: Hubbard U Instead of Stoner I. *Phys. Rev. B: Condens. Matter Mater. Phys.* **1991**, *44* (3), 943−954.

(66) Dudarev, S. L.; Botton, G. A.; Savrasov, S. Y.; Humphreys, C. J.; Sutton, A. P. Electron-Energy-Loss Spectra and the Structural Stability of Nickel Oxide: An LSDA+U Study. *Phys. Rev. B: Condens. Matter Mater. Phys.* **1998**, *57* (3), 1505−1509.

(67) Sun, J.; Ruzsinszky, A.; Perdew, J. P. Strongly Constrained and Appropriately Normed Semilocal Density Functional. *Phys. Rev. Lett.* **2015**, *115* (3), 036402.

(68) Monkhorst, H. J.; Pack, J. D. Special Points for Brillouin-Zone Integrations. *Phys. Rev. B* **1976**, *13* (12), 5188−5192.

(69) Curnan, M. T.; Kitchin, J. R. Effects of Concentration, Crystal Structure, Magnetism, and Electronic Structure Method on First-Principles Oxygen Vacancy Formation Energy Trends in Perovskites. *J. Phys. Chem. C* **2014**, *118* (49), 28776−28790.

(70) Hellenbrandt, M. The Inorganic Crystal Structure Database (ICSD)—Present and Future. *Crystallogr. Rev.* **2004**, *10* (1), 17−22.

(71) Ong, S. P.; Richards, W. D.; Jain, A.; Hautier, G.; Kocher, M.; Cholia, S.; Gunter, D.; Chevrier, V. L.; Persson, K. A.; Ceder, G. Python Materials Genomics (Pymatgen): A Robust, Open-Source Python Library for Materials Analysis. *Comput. Mater. Sci.* **2013**, *68*, 314−319.

(72) Slater, J. C. Atomic Radii in Crystals. *J. Chem. Phys.* **1964**, *41* (10), 3199−3204.

(73) Chu, I.-H.; Roychowdhury, S.; Han, D.; Jain, A.; Ong, S. P. Predicting the Volumes of Crystals. *Comput. Mater. Sci.* **2018**, *146*, 184−192.

(74) Xia, H.; Dai, J.; Xu, Y.; Yin, Y.; Wang, X.; Liu, Z.; Liu, M.; McGuire, M. A.; Li, X.; Li, Z.; et al. Magnetism and the Spin State in Cubic Perovskite $CaCoO_3$ Synthesized under High Pressure. *Phys. Rev. Mater.* **2017**, *1* (2), 024406.

(75) Vanysek, P. Electrochemical Series. In *CRC Handbook of Chemistry and Physics*; Haynes, W. M., Ed.; CRC Press: Boca Raton, FL, 2006; pp 20−29.

(76) Aydinol, M. K.; Kohan, A. F.; Ceder, G.; Cho, K.; Joannopoulos, J. Ab Initio Study of Lithium Intercalation in Metal Oxides and Metal Dichalcogenides. *Phys. Rev. B: Condens. Matter Mater. Phys.* **1997**, *56* (3), 1354−1365.

(77) Deml, A. M.; Holder, A. M.; O'Hayre, R. P.; Musgrave, C. B.; Stevanović, V. Intrinsic Material Properties Dictating Oxygen Vacancy Formation Energetics in Metal Oxides. *J. Phys. Chem. Lett.* **2015**, *6* (10), 1948−1953.

(78) Turnbull, D. Metastable Structures in Metallurgy. *Metall. Trans. B* **1981**, *12* (2), 217−230.

(79) Gopalakrishnan, J. Chimie Douce Approaches to the Synthesis of Metastable Oxide Materials. *Chem. Mater.* **1995**, *7* (7), 1265−1275.

(80) Aykol, M.; Dwaraknath, S. S.; Sun, W.; Persson, K. A. Thermodynamic Limit for Synthesis of Metastable Inorganic Materials. *Sci. Adv.* **2018**, *4* (4), eaaq0148.

(81) Sun, W.; Dacek, S. T.; Ong, S. P.; Hautier, G.; Jain, A.; Richards, W. D.; Gamst, A. C.; Persson, K. A.; Ceder, G. The Thermodynamic Scale of Inorganic Crystalline Metastability. *Sci. Adv.* **2016**, *2* (11), e1600225.

(82) Sun, W.; Bartel, C. J.; Arca, E.; Bauers, S. R.; Matthews, B.; Orvañanos, B.; Chen, B.-R.; Toney, M. F.; Schelhas, L. T.; Tumas, W.; et al. A Map of the Inorganic Ternary Metal Nitrides. *Nat. Mater.* **2019**, *18* (7), 732−739.

(83) Gautam, G. S.; Canepa, P.; Malik, R.; Liu, M.; Persson, K.; Ceder, G. First-Principles Evaluation of Multi-Valent Cation Insertion into Orthorhombic V_2O_5. *Chem. Commun.* **2015**, *51*, 13619−13622.

(84) Kang, C.-J.; Kotliar, G. Material Design of Indium-Based Compounds: Possible Candidates for Charge, Valence, and Bond Disproportionation and Superconductivity. *Phys. Rev. Mater.* **2019**, *3* (1), 015001.

(85) Hu, Q.; Yue, B.; Shao, H.; Yang, F.; Wang, J.; Wang, Y.; Liu, J. Facile Syntheses of Cerium-Based $CeMO_3$ (M = Co, Ni, Cu) Perovskite Nanomaterials for High-Performance Supercapacitor Electrodes. *J. Mater. Sci.* **2020**, *55* (20), 8421−8434.

(86) Ritzmann, A. M.; Muñoz-García, A. B.; Pavone, M.; Keith, J. A.; Carter, E. A. Ab Initio DFT+U Analysis of Oxygen Vacancy Formation and Migration in $La_{1-x}Sr_xFeO_{3-\delta}$ (x = 0, 0.25, 0.50). *Chem. Mater.* **2013**, *25* (15), 3011−3019.

(87) Grundy, A. N.; Hallstedt, B.; Gauckler, L. J. Assessment of the La−Sr−Mn−O System. *CALPHAD: Comput. Coupling Phase Diagrams Thermochem.* **2004**, *28* (2), 191−201.

(88) Nitadori, T.; Ichiki, T.; Misono, M. Catalytic Properties of Perovskite-Type Mixed Oxides (ABO_3) Consisting of Rare Earth and 3d Transition Metals. The Roles of the A- and B-Site Ions. *Bull. Chem. Soc. Jpn.* **1988**, *61* (3), 621−626.

(89) Muñoz-García, A. B.; Pavone, M.; Ritzmann, A. M.; Carter, E. A. Oxide Ion Transport in $Sr_2Fe_{1.5}Mo_{0.5}O_{6-\delta}$, a Mixed Ion-Electron Conductor: New Insights from First Principles Modeling. *Phys. Chem. Chem. Phys.* **2013**, *15* (17), 6250.

(90) Matsukawa, M.; Tamura, A.; Yamato, Y.; Kumagai, T.; Nimori, S.; Suryanarayanan, R. Thermal Transport in Electron-Doped Manganites. *J. Magn. Magn. Mater.* **2007**, *310* (2), e283−e285.

(91) Toher, C.; Oses, C.; Hicks, D.; Curtarolo, S. Unavoidable Disorder and Entropy in Multi-Component Systems. *npj Comput. Mater.* **2019**, *5* (1), 69.

(92) Andersson, D. A.; Simak, S. I.; Johansson, B.; Abrikosov, I. A.; Skorodumova, N. V. Modeling of CeO_2, Ce_2O_3, and CeO_{2-x} in the LDA+U Formalism. *Phys. Rev. B: Condens. Matter Mater. Phys.* **2007**, *75* (3), 035109.

(93) Nowotny, M. K.; Sheppard, L. R.; Bak, T.; Nowotny, J. Defect Chemistry of Titanium Dioxide. Application of Defect Engineering in Processing of TiO_2 -Based Photocatalysts. *J. Phys. Chem. C* **2008**, *112* (14), 5275−5300.

(94) Tuller, H. L.; Nowick, A. S. Defect Structure and Electrical Properties of Nonstoichiometric CeO2 Single Crystals. *J. Electrochem. Soc.* **1979**, *126* (2), 209.

(95) Chiang, Y.-M.; Lavik, E. B.; Kosacki, I.; Tuller, H. L.; Ying, J. Y. Defect and Transport Properties of Nanocrystalline CeO2−x. *Appl. Phys. Lett.* **1996**, *69*, 185.

(96) Chapman, D. M. Behavior of Titania-Supported Vanadia and Tungsta SCR Catalysts at High Temperatures in Reactant Streams: Tungsten and Vanadium Oxide and Hydroxide Vapor Pressure Reduction by Surficial Stabilization. *Appl. Catal., A* **2011**, *392* (1−2), 143−150.

(97) Caplan, D.; Cohen, M. The Volatilization of Chromium Oxide. *J. Electrochem. Soc.* **1961**, *108* (5), 438.

(98) Curnan, M. T.; Kitchin, J. R. Investigating the Energetic Ordering of Stable and Metastable TiO_2 Polymorphs Using DFT+ U and Hybrid Functionals. *J. Phys. Chem. C* **2015**, *119* (36), 21060−21071.

(99) Sanchez, J. M. Cluster Expansions and the Configurational Energy of Alloys. *Phys. Rev. B: Condens. Matter Mater. Phys.* **1993**, *48* (18), 14013−14015.

(100) Deml, A. M.; Stevanović, V.; Muhich, C. L.; Musgrave, C. B.; O'Hayre, R. Oxide Enthalpy of Formation and Band Gap Energy as Accurate Descriptors of Oxygen Vacancy Formation Energetics. *Energy Environ. Sci.* **2014**, *7* (6), 1996−2004.

(101) Muhich, C.; Steinfeld, A. Principles of Doping Ceria for the Solar Thermochemical Redox Splitting of H_2O and CO_2. *J. Mater. Chem. A* **2017**, *5* (30), 15578−15590.

(102) Muhich, C. L.; Ehrhart, B. D.; Witte, V. A.; Miller, S. L.; Coker, E. N.; Musgrave, C. B.; Weimer, A. W. Predicting the Solar Thermochemical Water Splitting Ability and Reaction Mechanism of Metal Oxides: A Case Study of the Hercynite Family of Water Splitting Cycles. *Energy Environ. Sci.* **2015**, *8* (12), 3687−3699.

(103) Balachandran, P. V.; Emery, A. A.; Gubernatis, J. E.; Lookman, T.; Wolverton, C.; Zunger, A. Predictions of New ABO_3 Perovskite Compounds by Combining Machine Learning and Density Functional Theory. *Phys. Rev. Mater.* **2018**, *2* (4), 043802.

(104) Bartel, C. J.; Millican, S. L.; Deml, A. M.; Rumptz, J. R.; Tumas, W.; Weimer, A. W.; Lany, S.; Stevanović, V.; Musgrave, C. B.; Holder, A. M. Physical Descriptor for the Gibbs Energy of Inorganic Crystalline Solids and Temperature-Dependent Materials Chemistry. *Nat. Commun.* **2018**, *9* (1), 4168.